Second Sound Scattering
In Superfluid Helium

Thesis by
Thomas Rösgen

In Partial Fulfillment
of the Requirements for the Degree of
Doctor of Philosophy

California Institute of Technology
Pasadena, California

1985
(Submitted 25 Sept. 1984)

ACKNOWLEDGEMENTS

I would like to thank first of all my advisor, Prof. H.W. Liepmann. His constant insight and support were crucial for the project throughout the years. Most important, though, he encouraged an approach to research based on intuition, self-motivation - and fun.

My further thanks go to Dr. J.R. Torczynski. As another member of the helium group and fellow student during many years, he was always a competent and patient judge of new ideas.

Finally, I am grateful to all the members of the GALCIT community, of Caltech and the Jet Propulsion Laboratory, without whose help and expertise at one time or another the continuation of the project would not have been possible.

This research was supported by NSF Grant No. MEA 82-00027 and Caltech funds.

ABSTRACT

Focusing cavities are used to study the scattering of second sound in liquid helium II. The special geometries reduce wall interference effects and allow measurements in very small test volumes.

In a first experiment, a double elliptical cavity is used to focus a second sound wave onto a small wire target. A thin film bolometer measures the side scattered wave component. The agreement with a theoretical estimate is reasonable, although some problems arise from the small measurement volume and associated alignment requirements.

A second cavity is based on confocal parabolas, thus enabling the use of large planar sensors. A cylindrical heater produces again a focused second sound wave. Three sensors monitor the transmitted wave component as well as the side scatter in two different directions. The side looking sensors have very high sensitivities due to their large size and resistance. Specially developed cryogenic amplifiers are used to match them to the signal cables.

In one case, a second auxiliary heater is used to set up a strong counterflow in the focal region. The second sound wave then scatters from the induced fluid disturbances.

Attempts to observe scattering from quantized vortex lines in the rotating parabolic cavity ultimately did not succeed, although a theoretical estimate seems to indicate a basic feasibility.

TABLE OF CONTENTS

LIST OF FIGURES

Chapter 1

INTRODUCTION

This thesis summarizes the results of an investigation on second sound scattering in liquid helium II. The initial idea was to develop a new measurement technique which would allow localized, nonintrusive measurements of flow properties in the superfluid. In this context, the propagation of waves and the subsequent measurement and analysis of their modification appeared to be an attractive choice.

Several experiments can be found in the literature which explored this concept in various ways. Mercereau et al. [1] used an array of heaters to produce second sound diffraction patterns in the superfluid. By this means, an accurate determination of the wavespeed as function of temperature was possible. Attempts to record effects due to the presence of quantized vortex lines were unsuccessful, however. Laguna [2] measured the attenuation of a second sound beam passing through a counterflow jet in order to investigate certain questions regarding supercritical helium flow and mutual friction. A similar technique was employed by Barenghi [3] to study "Quantum Turbulence." Here, the sound attenuation was used to determine the collective properties of quantized vortex "tangles." Turner [4] used the propagation of second sound shock waves to study intrinsic critical counterflow velocities in the superfluid. The time-of-flight technique using shock waves was also deployed by Borner et al. [5] to measure the circulation of large vortex rings in helium II. Finally, second sound shock waves were used again by Torczynski [6] in an effort to understand the role of quantized vortex lines in the superfluid breakdown.

All these concepts were incorporated in the plan to study second sound scattering as an underlying fundamental problem. To give the investigation a long-term objective, it was decided to attempt the observation of scattering from quantized vortex lines, if possible from a single line. Vortices appear to be connected to many of the unresolved questions in the understanding of superfluid helium. To point only in one direction, the phenomenon known as "mutual friction" is being interpreted as the interaction of vortex lines with the normal fluid component (see appendix C). Scattering experiments performed with the ability to distinguish the individual lines could be very useful as a check for existing theories. So far, the experiments of Williams, Packard et al. [7-9] represent the only direct visualization of a small number of lines, using a very sophisticated ion-drift technique. Recent developments in the field of (conventional) ultrasonic flow diagnostics (see for example [10]) seemed to indicate that an imaging of the lines by means of second sound is possible, provided the scattering is sufficiently strong.

The experiments described in the following chapters were designed to address various aspects of the scattering/imaging problem. The first setup uses a double elliptical cavity to look at scattering from a solid wire target. It serves mainly as a check for the concept of focused second sound, which is used to achieve high spatial selectivity. The results compare quite well with a theoretical estimate and led to the design of a new, improved cavity based on confocal parabolas. This second geometry is optimized for the observation of scattering from fluid disturbances, involving newly designed high-sensitivity bolometers. A counterflow can be induced in the focal volume and its interaction with a probing wave leads to a measurable scattering response. Finally, a theoretical estimate is derived for the scattering from a quantized vortex line and indicates the basic feasibility of such an experiment. Attempts to observe a signal from the lines in the parabolic cavity were however inconclusive.

References

1. Mercereau, J., Notarys, H. and Pellam, J.R., *Diffraction of Heat Waves in Stationary and Rotating Liquid Helium* , Proc. VII Int. Conf. on Low Temperature Physics, Univ. of Toronto (1960).

2. Laguna, G., *Second Sound Attenuation in a Liquid Helium Counterflow Jet*, Ph.D. Thesis, Aeronautics, Caltech (1975).

3. Barenghi, C., *Experiments on Quantum Turbulence*, Ph.D. Thesis, Physics, Univ. of Oregon (1982).

4. Turner, T., *Using Second Sound Shock Waves to Probe the Intrinsic Critical Velocity of Liquid Helium II*, Phys. Fluids **26**, 11 (1983).

5. Borner, H., Schmeling, T. and Schmidt, D., *Experiments on the Circulation and Propagation of Large-Scale Vortex Rings in He II*, Phys. Fluids **26**, 6 (1983).

6. Torczynski, J., *Second Sound Shock Waves in Rotating Superfluid Helium*, Ph.D. Thesis, Aeronautics, Caltech (1983).

7. Williams, G. and Packard, R., *Photographs of Quantized Vortex Lines in Rotating He II*, Phys. Rev. Lett. **33**, 5 (1974).

8. Williams, G. and Packard, R., *A Technique for Photographing Vortex Positions in Rotating Superfluid Helium*, J. Low Temp. Phys. **39**, 5 (1979).

9. Yarmchuck, E. and Packard, R., *Photographic Studies of Quantized Vortex Lines*, J. Low Temp. Phys. **46**, 5 (1981).

10. Trebitz, B. *Acoustic Transmission Imaging for Flow Diagnostics*, Ph.D. Thesis, Aeronautics, Caltech (1982).

Chapter 2

THE ELLIPTICAL CAVITY

We start out with the description of an experiment which was designed to study a relatively simple problem: scattering from a solid cylinder. The second sound cavity was also intended as a testbed for various novel features which seemed desirable for the investigation of other scattering phenomena with higher sensitivity and resolution requirements.

2.1. Geometry and Focusing Behaviour

In Figure 2.1, a sketch of the basic geometry of the experiment is given. It consists of two confocal elliptical sections, which serve as the reflecting sidewalls of a closed resonator. The set-up is two-dimensional in that the sidewalls are straight in the z-direction. Cylindrical waves created in one of the focal points, say 1, will propagate toward the other two centers (2,3). Since all pathlengths are equal, the waves will refocus again, preserving their cylindrical character.

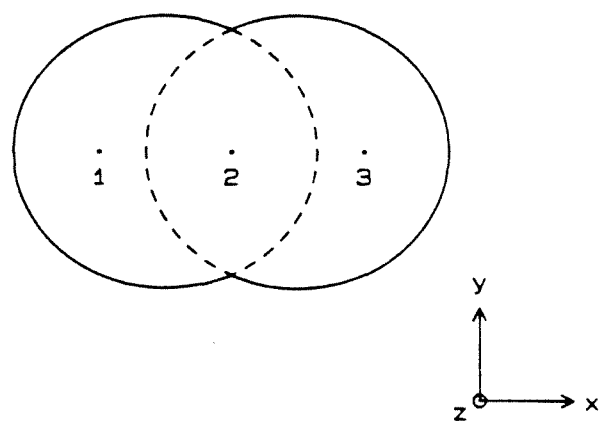

Figure 2.1. Schematic of the double elliptical cavity.

Using diffraction theory (see Sommerfeld [1]), it can be shown that the focal region in a cylindrical wave has an elliptical shape. The typical dimensions are

$$\Delta x \propto \lambda \left[\frac{F}{D} \right]^2$$

in the direction of wave propagation, and

$$\Delta y \propto \lambda \left[\frac{F}{D} \right]$$

in the perpendicular direction (see Figure 2.2). Here λ is the wavelength of the incident wave, F the effective distance between the generating aperture and the focus, and D the aperture size. The constants of proportionality are of order unity.

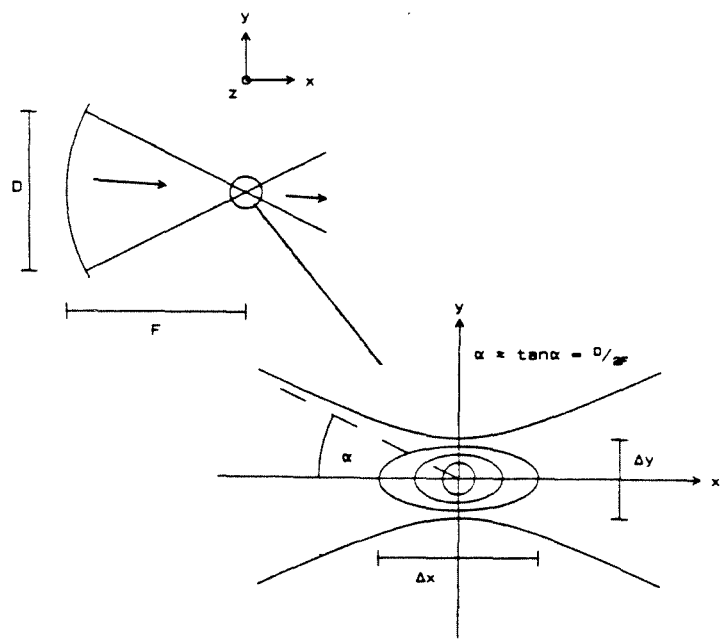

Figure 2.2. Geometry of a cylindrical focus.

The wave strengthens as it focuses, and with the appropriate choice for F and D, the high intensity region in the focus can be made as small as a few wavelengths. This behaviour is used in the experiment to create a very small observation volume which is located away from the interfering sidewalls and heater/detector surfaces.

Figure 2.3 shows the heater and sensor positioned in focal points 1 and 3. Both have cylindrical surfaces and are thus matched to the local curvature of the wavefronts or eigenmodes propagating in the cavity. The heater H focuses on the target T from the left, whereas the sensor S "looks" at the same area from the right. Due to the reciprocity principle, the sensor may be treated as if it were sending out a wave, too.

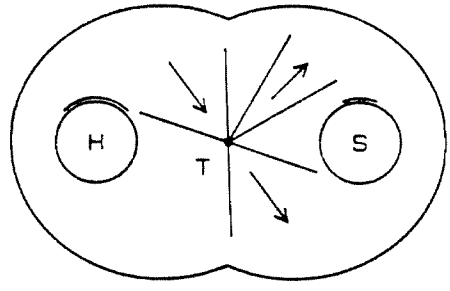

Figure 2.3. The cavity geometry. The lines and arrows indicate the approximate direction and size of the incident and observed scattered waves.

The finite size of the heater surface (compared to, say, a line source) has the advantage that the intensity of the emitted wave reaches its peak in the target area: everywhere else it is significantly smaller. Using the notation introduced

introduced above, the increase in the wave intensity is given by the ratio of the beam width at the heater (D) and at the focus (Δy). This becomes

$$\frac{I_{focus}}{I_{heater}} = \frac{D}{\Delta y} \approx \frac{D^2}{\lambda F}.$$

The actual ratio for the experiment is between 10 and 120, depending on the wavelength.

For the sensor, the main advantage of a finite size lies in the fact that the resistance - and thus the sensitivity - can be increased. This aspect will be discussed in more detail in the next section.

Since only segments of the heater and sensor surfaces are used, the incident wave cannot be "seen" by the sensor. Only a cylindrical, side scattered wave out of the target region will be registered. This feature is ideal for the recording of weak signals, because the incident wave does not mask the scattered components. The specific arrangement also has another advantage. The focal lobes (see Fig. 2.2) of the transmitter and receiver overlap at almost right angles. Thus, their combined amplitude distributions create an area of maximum sensitivity which has a near circular shape. The asymmetry of a single cylindrical focus is no longer present.

Figures 2.4a to 2.4e summarize the results of some calculations for the sensitivity pattern in the central focus. The actual cavity parameters of the experiment were used in the program. Figure 2.4a displays the shape of the focus as created by the incident wave, Figure 2.4b the pattern associated with the sensor. The product of both functions, Figure 2.4c, gives the total spatial selectivity. All plots are scaled to a peak value of 1.0 at the center, since only the spatial shape is of interest. The x- and y-dimensions are normalized with the wavelength. The

contour increment is 0.1 and there are 10 levels between 0.0995 and 0.995. Since the calculations include to some extent the diffraction effects due to the finite heater and sensor, the results have a slight dependence on the actual wavelength and are not symmetric with respect to the centerline. Figures 2.4d and 2.4e show the same function as 2.4c, but for different values of the wavelength λ.

The dashed lines in all the plots define the geometric "size" of the heater and sensor waves, derived from the solid angle subtended by their respective apertures. The circles in the center of the plots indicate the diameter of a typical target cylinder, with the ratio ξ, the radius scaled by the wavelength, given in the captions. Note the relative size especially in the high wavenumber case (Fig. 2.4e). For these short wavelengths, the alignment of the cylinder in the focal point becomes quite important. The somewhat square shape of the focal peak is due to the different lateral widths of the heater and sensor patterns.

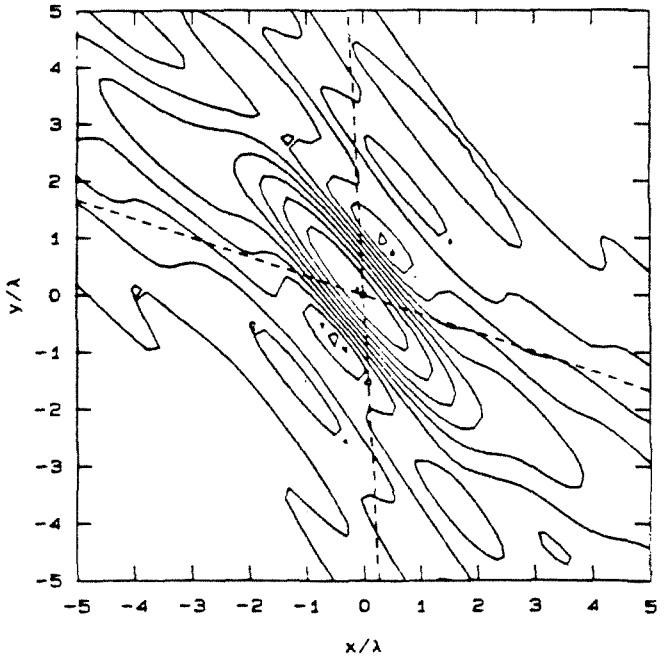

Figure 2.4a. Diffraction pattern of the incident wave near the focus.

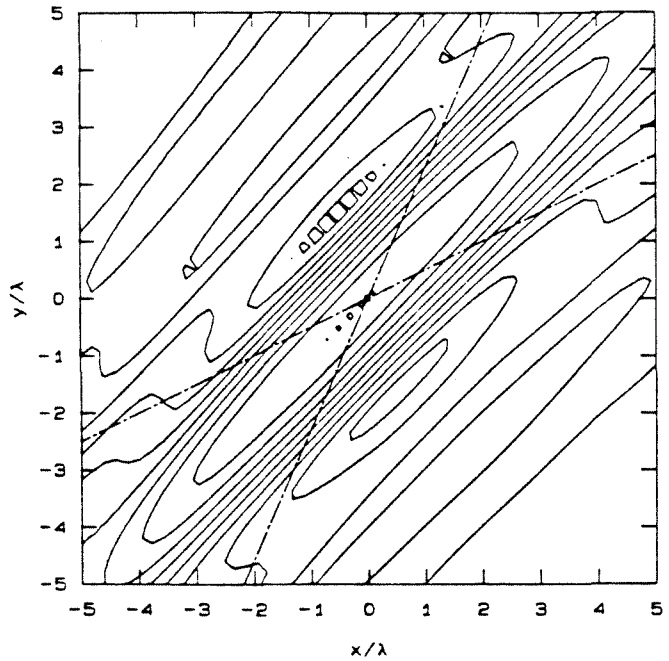

Figure 2.4b. Diffraction pattern of the sensor near the focus.

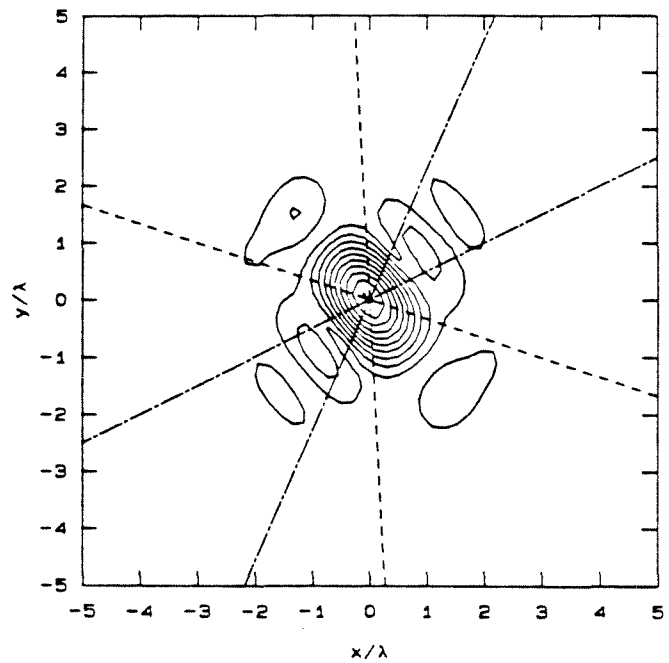

Figure 2.4c. Total spatial selectivity of the cavity. The dimensionless cylinder radius is ξ=0.051 (see text).

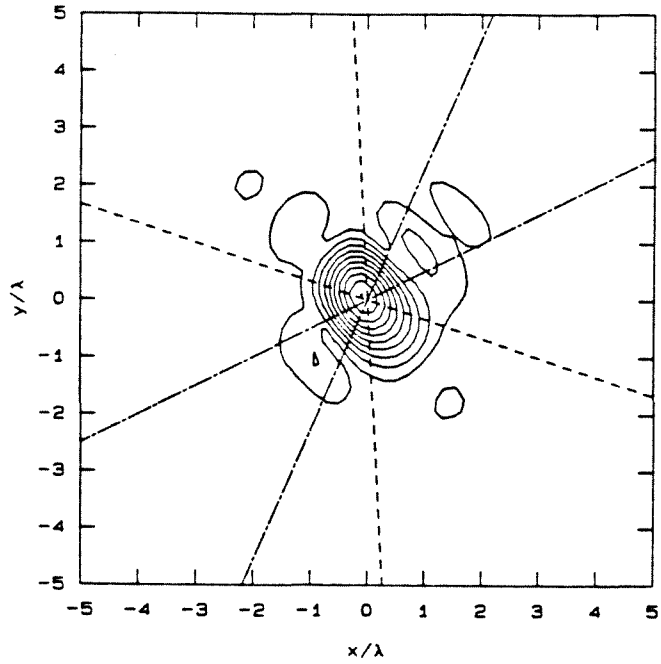

Figure 2.4d. same as Figure 2.4c, but ξ=0.01.

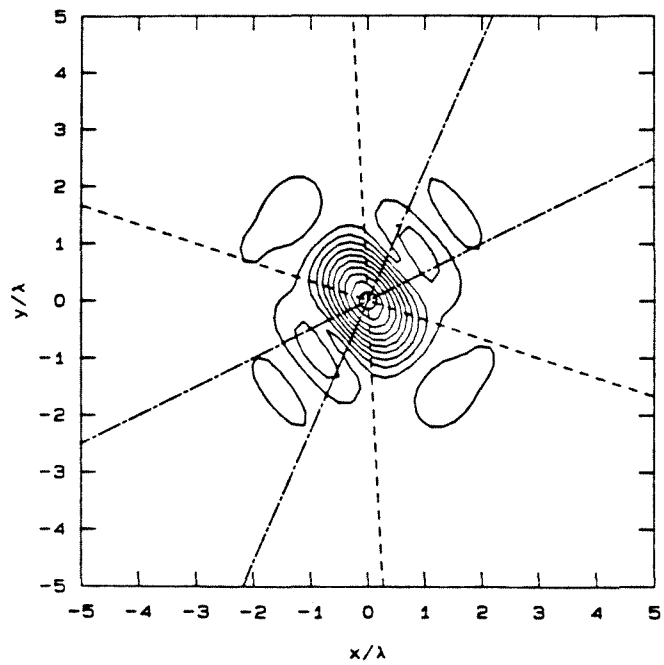

Figure 2.4e. same as Figure 2.4c, but ξ=0.152.

To summarize, the choice of a double elliptical cavity determines the following properties of the scattering experiment:

— The incident wave as well as the sensor field of view are focused.

— The probing area, as defined by the maximum sensitivity pattern, is on the order of a few wavelengths.

— The sensor does not record the incident wave.

— The target area is away from solid surfaces; thus "non-intrusive" measurements are possible.

2.2. Fabrication and Physical Dimensions

The actual cavity was cut out of a single brass rod by a computer-controlled milling machine. This assures the high dimensional accuracy required for the resonator geometry. The step size and tool diameter were such that the cavity sidewalls have a surface finish that is smooth compared to typical second sound wavelengths. More details on the machining and programming are given in appendix A.

The depth of the cavity is 0.5", its maximum width 1.75", and the half axis ratio of the ellipses 0.9. This results in a spacing between the foci of 0.531". Note in this context that the drawing in Figure 2.3 reproduces the actual proportions of the design.

The heater and sensor cylinders are formed by quartz tubing of 0.326" outer diameter. The cylinders are centered by solid brass cores which in turn are rigidly mounted on the cavity top plate. The cavity floor has two circular recesses into which the heater and sensor assemblies plug, enforcing the proper alignment. Figure 2.5 shows a photograph of the top and bottom pieces of the cavity. The leads for the heater and sensor are inside the two cylinders, keeping

the exposed surfaces in the cavity "clean" in the geometric sense. Special care was taken to assure that the endplates of the two columns are flush with the cavity bottom. The gaps between the glass and brass pieces are filled with self-leveling silicone rubber cement.

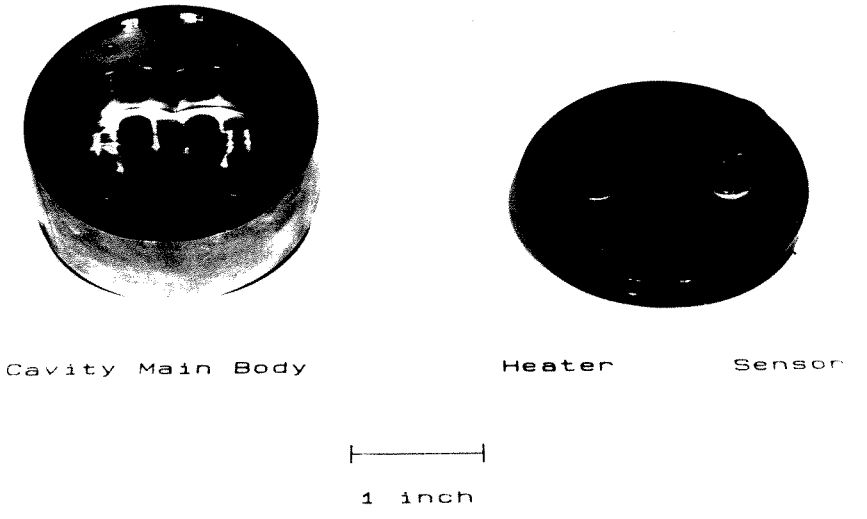

Figure 2.5. Photograph of the elliptical cavity.

The heater is a Nichrome thin film deposited over the whole length of the quartz cylinder and covering an angle of 90 degrees. Its thickness was chosen to yield a resistance of about 100 Ω (actual value 113 Ω). As described already, contact is made by copper film leads and superconducting wire at the very ends of the cylinder, which protrude outside the cavity.

The sensor, on the other hand, is a granular aluminum thin film about .05" wide in the middle of the glass column. It covers an angle of approximately 60 degrees. The technique of changing the transition temperature of aluminum

bolometers by using oxygen is described in Wise's [2] thesis and will not be discussed further. Due to spatial limitations, no magnets are provided in the set-up to modify the intrinsic transition temperature, thus limiting the experimental runs to a very small temperature range. Contact to the sensor strip is made by two copper thin films, which extend to the ends of the cylinder. There, again, superconducting wire connects these leads to the outside cables.

A major objective in the experiment was to check the performance of high resistivity sensors. The sensitivity (in Volt/Kelvin) of a superconducting transition edge bolometer is proportional to the current and the resistance. Using R_n as the normal resistance and R as the resistance during the transition one can define an intrinsic sensitivity (independent of R_n):

$$\alpha := \frac{1}{R_n} \frac{dR}{dT} .$$

Biasing the sensor with a constant current I_0, the voltage readout due to a temperature fluctuation ΔT becomes

$$\Delta V = \alpha I_0 R_n \Delta T .$$

Since the dissipation is quadratic in I_0 but only linear in R_n, its is better to increase the resistance to obtain high sensitivity.

Scribing the film surface to increase the effective sensor length, the resistance was pushed up to 53.2 kΩ , compared to the more common values of about 100 Ω to 1 kΩ for layered tin-on-gold films. The choice of granular aluminum as the sensor material was made because of the high "geometric" film resistance (10 Ω /square vs. 0.5 Ω /square for Sn-Au). Using a bias current of 50 μA, sensitivities of around 70 Volt/Kelvin were achieved. The problems associated with

the capacitive loading of a high resistance sensor will be discussed in chapter 4 and in appendix B.

The target area was designed for easy exchange of the scattering objects. Located in the focal point are threaded (2-56) holes, into which guiding screws are inserted. The screws are made out of nylon and contain a small metal channel (25G disposable needle). The target cylinders (or better: wires) reach the cavity interior through these channels. Care was again taken to assure flush surfaces between the screw heads and the cavity walls.

The target is formed, as indicated, by small metal wires, usually .0005" to .002" in diameter. Tension is put on these wires outside the cavity to keep them straight. The thicker ones are soldered to a phosphor-bronze leaf spring on one end and locked down on the other, whereas the thinner wires are loaded with little weights and straightened by gravity.

2.3. References

1. Sommerfeld, A., *Lectures in Theoretical Physics*, Vol. IV (Optics), Academic Press, New York (1954), p. 323 ff.

2. Wise, J., *Experimental Investigation of First- and Second-Sound Shock Waves in Liquid Helium II*, Ph.D. Thesis, Aeronautics, Caltech (1979).

Chapter 3

SECOND SOUND SCATTERING FROM A CYLINDER

In this chapter we will derive a theoretical estimate for the scattering of second sound from a solid cylinder. As will be evident from the calculations, the problem is equivalent to the scattering from a 'hard' cylinder in normal acoustics (see Morse & Ingard [1]). However, special attention must be paid to the boundary conditions at the solid/liquid interface.

3.1. Theoretical Derivation

Consider the situation depicted in Figure 3.1. A cylindrical wave *I* in a wedge with half angle ψ_0 impinges on a cylinder of diameter $2a$.

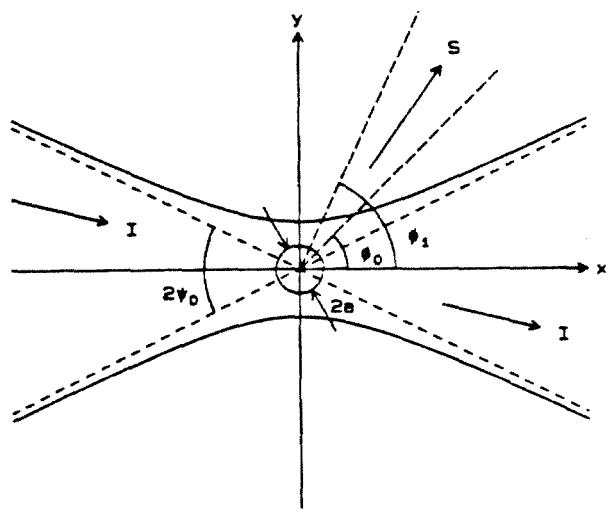

Figure 3.1. Geometry of the scattering problem.

The presence of the cylinder will modify the waveform and the difference between the unperturbed and perturbed waveforms is defined as the scattered wave S. A sensor picks up this radiation in a wedge defined by the angles φ_0 and φ_1. A cylindrical coordinate system (r,φ) is chosen to line up with the center of the cylinder.

We are looking at second sound waves, that is entropy or temperature perturbations propagating in superfluid helium. Thus, we choose temperature as the principal variable and write down a wave equation for the corresponding temperature perturbations T':

$$\frac{\partial^2 T'}{\partial t^2} - a_2^2 \nabla^2 T' = 0 . \tag{3.1}$$

Here $a_2 = \left(\frac{\rho_s}{\rho_n} \frac{s^2}{c_p} T \right)^{\frac{1}{2}}$ is the velocity of second sound, ρ_s and ρ_n are the unperturbed densities of the superfluid and normal components, s is the the ambient entropy, T the temperature and c_p the specific heat. We will not elaborate on the derivation of equation (3.1) at this point, as Chapter 7 gives an introduction to the two-fluid model in the context of vortex scattering.

The heat flow inside the cylinder is, of course, governed by a diffusion equation,

$$\frac{\partial T'}{\partial t} = \kappa \nabla^2 T' . \tag{3.2}$$

Here $\kappa = \frac{\lambda}{\rho_c c_{p,c}}$ denotes the thermal diffusivity of the solid, λ the thermal conductivity, ρ_c the density and $c_{p,c}$ the specific heat.

The boundary condition at the cylinder is determined by postulating the conservation of all the heat fluxes normal to the surface. There is a heat flow $\vec{q}_i$ due to the incident wave, a heat flow $\vec{q}_r$ in the scattered wave and a leakage flow $\vec{q}_c$ into the cylinder. The conservation condition is

$$q_i + q_r + q_c = 0 \qquad (r = a) \,. \tag{3.3a}$$

Here the vector notation has been omitted since we are looking only at the radial components of the heat flow.

In the superfluid, the heat flow is related to the temperature perturbation by the equation

$$\vec{q} = \frac{-i}{\omega} \rho \, a_2^2 \, c_p \, \nabla \, T' \,, \tag{3.3b}$$

where $\rho = \rho_s + \rho_n$ is the total helium density.

The heat transport in the cylinder is described by the Fourier conduction law

$$\vec{q}_c = - \lambda \nabla \, T' \,. \tag{3.3c}$$

Finally, there is a Kapitza resistance across the liquid/solid interface such that

$$q_c = \frac{1}{R_K} \left(T'_c - T'_i - T'_r \right) \,. \tag{3.3d}$$

R_K is the Kapitza resistance, a constant dependent on the actual solid and liquid involved.

Looking at equation (3.3a), one may estimate the magnitude of the various terms by substituting (3.3b) and (3.3c); a dimensionless parameter can be formed

$$\sigma = \frac{\alpha \lambda}{\rho c_p a_2} , \tag{3.4}$$

where $\alpha^2 = \frac{i\omega}{\kappa}$ results from matching the time dependence of the temperature fluctuations in the helium and the cylinder. The parameter represents the ratio of the heat "conductivities" of the solid and the superfluid helium. It turns out to be very small for the materials chosen in the actual experiment. This translates into a negligable heat flux q_c into the cylinder and the final, approximate boundary condition may be written as

$$q_i \approx -q_r \qquad (r = a) . \tag{3.5}$$

This is equivalent to the boundary condition for a "hard" cylinder in normal acoustics, where the sum of the incident and reflected radial wave velocities vanishes at the surface.

We now have to find a mathematical expression for the incident wave. As a simple approximation, we write it as the superposition of plane waves in a wedge with half angle ψ_0, centered along the negative x-axis (see Sommerfeld [2]):

$$T(r,\varphi) = T_0' \int_{\pi-\psi_0}^{\pi+\psi_0} e^{-ikr\cos(\varphi-\psi)}\, d\psi . \tag{3.6}$$

Here, as everywhere in the following, an $e^{-i\omega t}$ time dependence was assumed and will not be mentioned explicitly. Although this formulation does not take into

account the actual positioning of the heater in the cavity and the reflection of the second sound waves from the walls, the diffraction effects due to the finite-sized beam are incorporated.

The incident profile as described in (3.6) may be decomposed in a series of Bessel functions:

$$T(r,\varphi) = 2\ T_0' \sum_{m=0}^{\infty} \varepsilon_m\ (i)^m\ \frac{\sin(m\psi_0)}{m} \cos(m\varphi)\ J_m(kr)\ , \tag{3.7a}$$

where

$$\varepsilon_m = \begin{cases} 1 & m = 0 \\ 2 & m \neq 0\ . \end{cases} \tag{3.7b}$$

The asymptotic form of equation (3.7a) for large radii may be used to find an expression for the heater induced temperature fluctuations T_h' at an equivalent radius r_0 and $\varphi = \pi$:

$$T_h'(r_0) \approx\ T_0'\ \pi \left(\frac{2}{\pi k r_0} \right)^{\frac{1}{2}} e^{-i\left(kr_0 - \frac{\pi}{4}\right)}\ . \tag{3.8}$$

This resembles closely the asymptotic form of the Hankel function $H_0^{(2)}(kr_0)$, which represents an incoming cylindrical wave.

The scattered wave is similarly expanded in a series

$$T_s'(r,\varphi) = T_0' \sum_{m=0}^{\infty} B_m\ H_m^{(1)}(kr) \cos(m\varphi)\ . \tag{3.9}$$

The boundary condition (3.5) translates into matching the radial derivatives of (3.7) and (3.9). From this, one may solve for the unknown coefficients B_m:

$$B_m = -2\,\varepsilon_m\,(i)^m\,\frac{\sin(m\psi_0)}{m}\,\frac{J_m'(ka)}{H_m^{(1)\prime}(ka)}\,. \tag{3.10}$$

A sensor in helium registers twice the temperature fluctuation of the liquid because of the reflection boundary condition. Due to the symmetry of the cavity, the detector is assumed to be located also at the radius $r = r_0$. Averaging over the interval (φ_0,φ_1) of angles subtended by the sensing aperture, the scattering amplitude becomes with (3.9)

$$T_{sns}'(r_0,\varphi_0,\varphi_1) = 2\,T_0'\sum_{m=0}^{\infty} B_m\,H_m^{(1)}(kr_0)\,\frac{\sin(m\varphi_1)-\sin(m\varphi_0)}{m\,(\varphi_1-\varphi_0)}\,. \tag{3.11}$$

Using the asymptotic expansion of the Hankel function and substituting the B_m from equation (3.10), this may be written as

$$T_{sns}'(r_0,\varphi_0,\varphi_1) \approx -4\,T_0'\left[\frac{2}{\pi k r_0}\right]^{\frac{1}{2}} e^{\,i\left(kr_0-\frac{\pi}{4}\right)}\times \tag{3.12}$$

$$\left\{\sum_{m=0}^{\infty}\varepsilon_m\,\frac{J_m'(ka)}{H_m^{(1)\prime}(ka)}\,\frac{\sin(m\psi_0)}{m}\,\frac{\sin(m\varphi_1)-\sin(m\varphi_0)}{m\,(\varphi_1-\varphi_0)}\right\}.$$

Finally, one may normalize the sensor response with the heater temperature T_h' (3.8) to obtain the scattered signal magnitude:

$$\left| \frac{T_{sns}'}{T_h'} \right| = \frac{4}{\pi} \left| \sum_{m=0}^{\infty} \varepsilon_m \frac{J_m'(ka)}{H_m^{(1)\cdot}(ka)} \frac{\sin(m\psi_0)}{m} \frac{\sin(m\varphi_1) - \sin(m\varphi_0)}{m\,(\varphi_1 - \varphi_0)} \right| . \qquad (3.13)$$

Here the ε_m are given by equation (3.7b). The formula (3.13) was evaluated on a computer as a function of the dimensionless wavenumber ka, and the result is shown in figure (3.2). The values ψ_0= 34.24°, φ_0= 79.29° and φ_1= 119.08° were chosen to match the experiment.

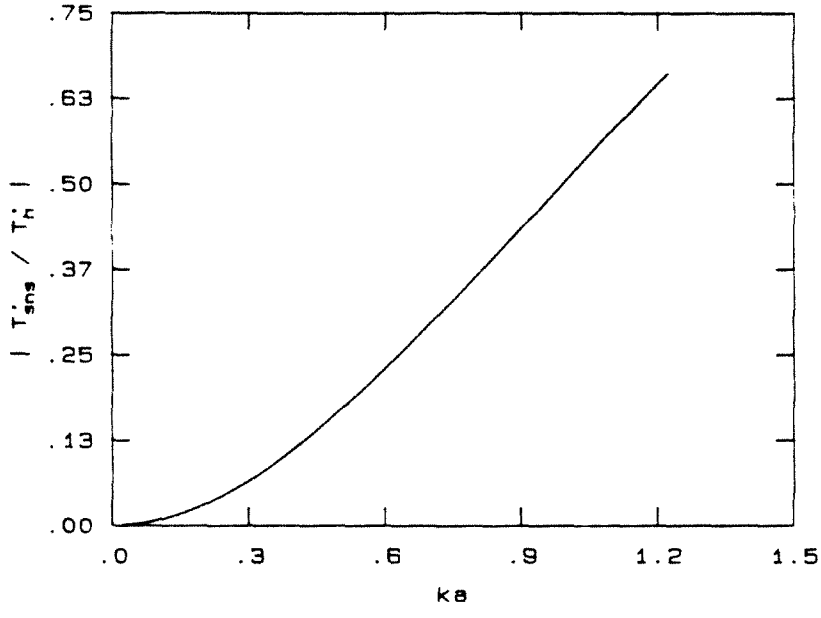

Figure 3.2. The scattering response from a solid cylinder.

3.2. References

1. Morse, P. and Ingard, K., *Theoretical Acoustics*, McGraw-Hill, New York (1968), p. 400 ff.

2. Sommerfeld, A., *Lectures on Theoretical Physics*, Vol. IV (Optics), Academic Press, New York (1954), p. 323 ff.

Chapter 4

EXPERIMENTAL SET-UP AND RESULTS

We proceed now with the description of the experimental set-up and the data aquisition system.

Since the cavity is essentially a resonator and the generated waves are eigen-modes, it is necessary to use burst-like signals to avoid resonances. Figure 4.1 shows a schematic of the heater pulse generation.

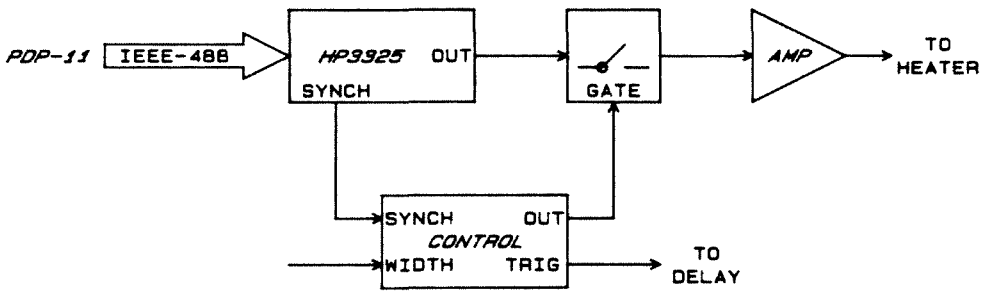

Figure 4.1. Schematic of the heater pulse generation.

A continuous sine wave is produced by a digital synthesizer (Hewlett Packard HP3325A) and fed into a fast semiconductor switch. This switch is controlled by a specially designed synchronization circuit. It accepts a trigger pulse and closes the switch for the duration of the pulse length signal. The opening and closing occur at the transition edges of the synchronization signal from the HP3325. This assures that the output sine wave is switched during the zero-crossings. An output current booster provides enough power to drive low resistance heaters

($\approx$ 10 Ω). The amplitude and frequency of the synthesizer are set by a PDP-11 minicomputer via an IEEE-488 interface. This enables the computer to sweep automatically over a prescribed range of scattering frequencies.

It should be pointed out that the heater produces temperature fluctuations by Joule heating and thus the excursions are only positive. Furthermore, the squaring of the input signal leads to frequency doubling and the generation of a "mean" square pulse with a superposed sinusoidal modulation.

The sensor electronics are sketched in Figure 4.2. A programmable current source (Keithley Model 225) in series with a 1 MΩ resistor is used to bias the sensor. The signal is received on the outside of the dewar by a guard amplifier, which eliminates the frequency-dependent loading effect otherwise present due to the cable capacitance. More details on this circuit and the loading problem are given in appendix B. Since the guard has unity gain, another amplifier (PAR 113, Princeton Applied Research) is used to boost the signal. Next, an analog high-pass filter (Krohn-Hite Model 3202) removes most of the low frequency fluctuations. Finally, the received waveform is sampled by a digital oscilloscope (Nicolet Explorer III) and transfered to the PDP-11 via the IEEE-488 interface. The triggering of the oscilloscope is performed by a variable digital delay with a programming accuracy of 100 ns. The delay is synchronized with the heater pulse generation so that the received signals are always phase-locked. This is essential because the sampled data are averaged by the PDP-11 to improve the signal-to-noise ratio.

The calibration curves for the sensor, one of which is shown in Figure 4.3, are generated by measuring the voltage drop across the sensor and the output voltage of an electronic manometer (Datametrics Barocel 1014) during a sweep through the transition region of the bolometer. Both pressure and sensor signals are sampled by a digital voltmeter (HP 5328A, Hewlett Packard) and

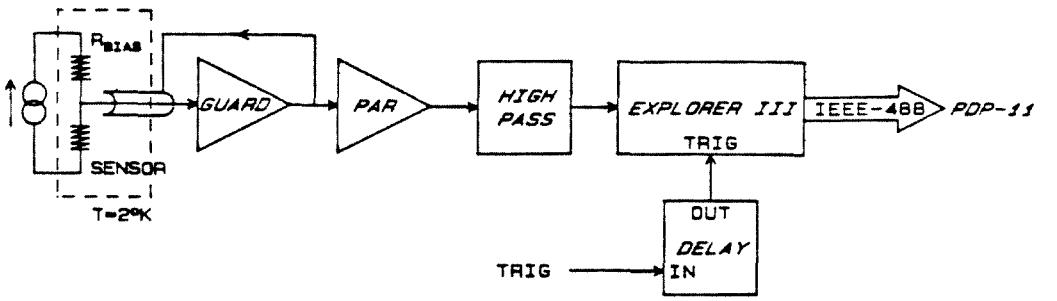

Figure 4.2. Schematic of the sensor electronics.

transferred to the computer for processing and plotting. The sensitivity shown in Figure 4.3 is computed as the average slope of the transition curve between the two cursor marks.

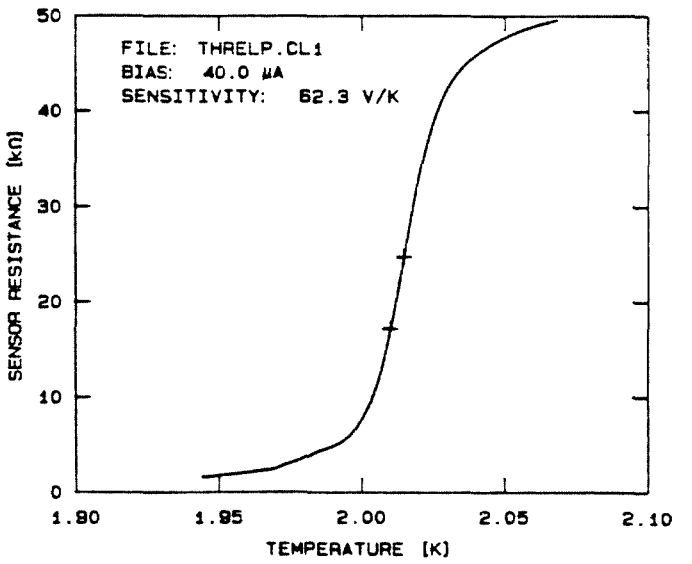

Figure 4.3. Typical calibration curve for the sensor.

The results which will be presented next were taken at T= 2.012 K. The heater pulse is a gated sine wave of 300 μs duration. This corresponds to a physical length of the pulse of 4.9 mm, which is much shorter than the path length for a round trip in the cavity. Due to the synchronization scheme described above, the exact pulse duration depends on the frequency chosen, because the last sinusoidal cycle after 300 μs is always completed. The sensor bias current is 40 μA, and the PAR amplifier operates at a gain of 2000, with the roll-off settings at 1 kHz and 300kHz. The high-pass cutoff of the analog filter is fixed at 10 kHz. The oscilloscope samples 1024 points at 2 MHz with 12 bit resolution, giving a 512 μs time record. The trigger delay is set to 3.32 ms so that the received burst signals are centered in the sampling window.

Figure 4.4 shows a typical waveform after the signal averaging. Most of the noise in the original signal has been removed, because averaging over N=200 sweeps improves the signal-to-noise ratio by a factor of $\sqrt{N} \approx 14$. The remaining fluctations of the burst envelope are due to the signature of the mean pulse and diffracted waves traveling in the cavity. The frequency used in this run is 100 kHz, and the heater voltage of 9.15 Volt peak-to-peak translates into a temperature fluctuation of 85 μK at the heater surface. We will use this waveform to demonstrate some of the steps in the data reduction.

The data processing first uses a quadrature detection scheme to determine the envelope of the signal. The signal may be written as

$$S(t) = E(t)\,\sin(\omega\, t\, +\, \varphi)$$

where $E(t)$ is the signal envelope, ω the (known) burst frequency and φ an arbitrary phase factor.

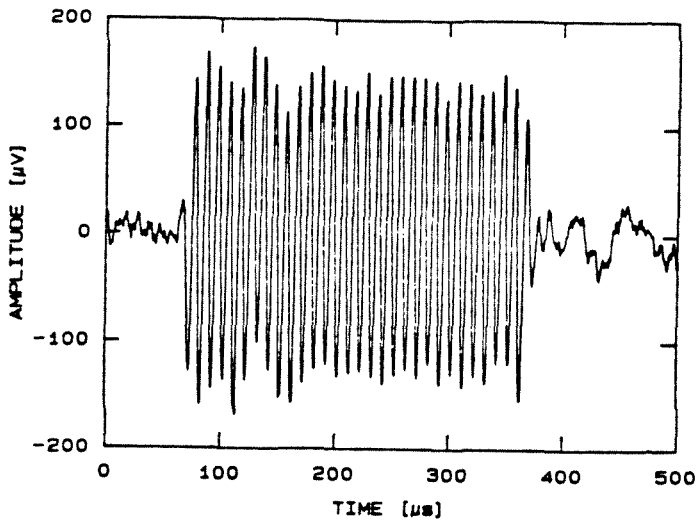

Figure 4.4. Received scattering waveform after signal averaging.

Multiplying by $\sin\omega t$ and $\cos\omega t$ yields

$$S_1(t) = \frac{1}{2} E(t) \left[(1 - \cos 2\omega t) \cos\varphi + \sin 2\omega t \sin\varphi \right]$$

$$S_2(t) = \frac{1}{2} E(t) \left[(1 + \cos 2\omega t) \sin\varphi + \sin 2\omega t \cos\varphi \right].$$

After low pass filtering with a cutoff at ω, the result becomes

$$\bar{S}_1(t) = \frac{1}{2} E(t) \cos\varphi$$

$$\bar{S}_2(t) = \frac{1}{2} E(t) \sin\varphi$$

and the envelope can be written as

$$E(t) = 2\sqrt{\bar{S}_1(t)^2 + \bar{S}_2(t)^2}\,.$$

The result of such a filter operation is shown in Figure 4.5. Note that the shifts in the original envelope are no longer visible. This means that they do not affect the amplitude of the harmonic signal component. Thus the pulse accompanying the sine wave in the heater signal does not seem to influence the scattering at high frequencies.

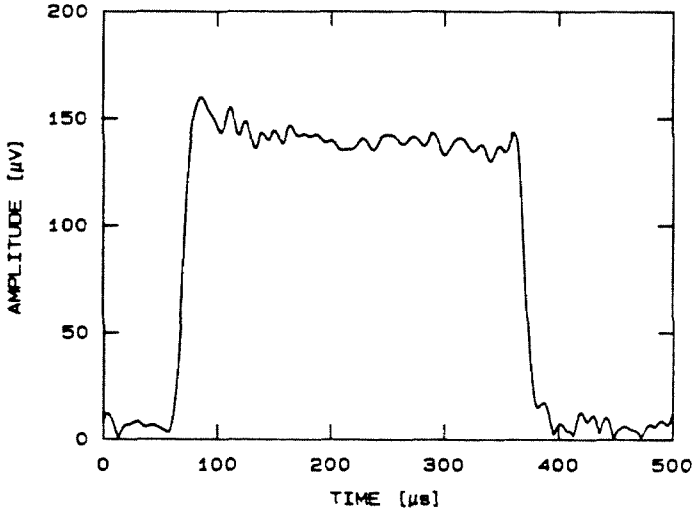

Figure 4.5. Envelope detection.

The next processing step is the computation of an amplitude histogram for the envelope, in which a peak appears at the average burst amplitude level (Figure 4.6). A weighted average around this peak then yields the final measure of the amplitude. This procedure makes the data processing quite insensitive to the residual noise in the signal. The choice for the averaging interval in the histogram is made by the operator. However, the selected threshold values do not change significantly for the various traces.

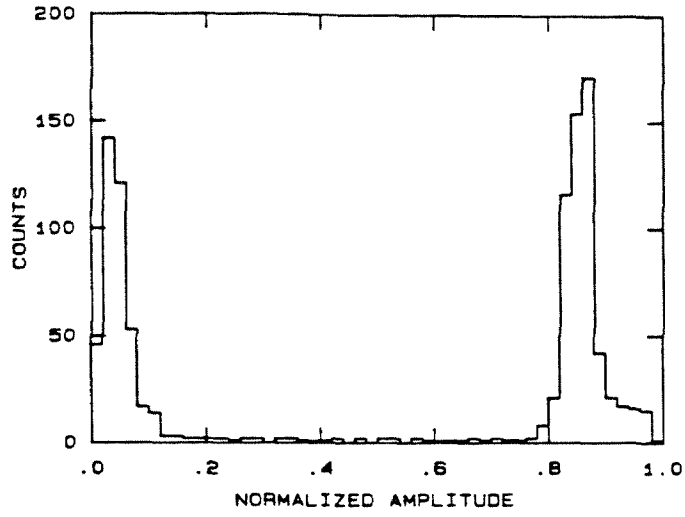

Figure 4.6. Normalized amplitude histogram of the waveform in Fig. 4.5

A first set of data was taken to determine whether the observed scattering occured in the linear, small amplitude regime. For this, two frequency sweeps were performed from 20 kHz to 200 kHz in 10 kHz steps. The heater amplitude was changed between the runs so as to increase the incident wave strength by a factor of two. If the scattering is linear in the prescribed amplitude range, the heater amplitude according to equation (3.13) should scale out and both normalized scattering curves should collapse. Figure 4.7 shows the result of plotting the two scans in normalized coordinates. There seems to be some discrepancy between the two cases, with the higher amplitude case resulting from the stronger incident wave. However, one notices a reversal of this trend at low frequencies, which makes a consistent explanation difficult. If a nonlinearity were present, one should expect a *reduction* of the scaled scattering amplitude at the incident frequency. The scattering energy would go into the creation of higher harmonics and remain undetected by the filtering scheme employed. A potential source of error is the difference in the original signal-to-noise ratio

for the two runs. The lower amplitude case has of course a smaller signal component and this might lead to a degradation of the average amplitude, at least if phase noise is considered. Thus, it appears that nonlinearity, especially due to the wave focusing, does not affect the observed scattering significantly.

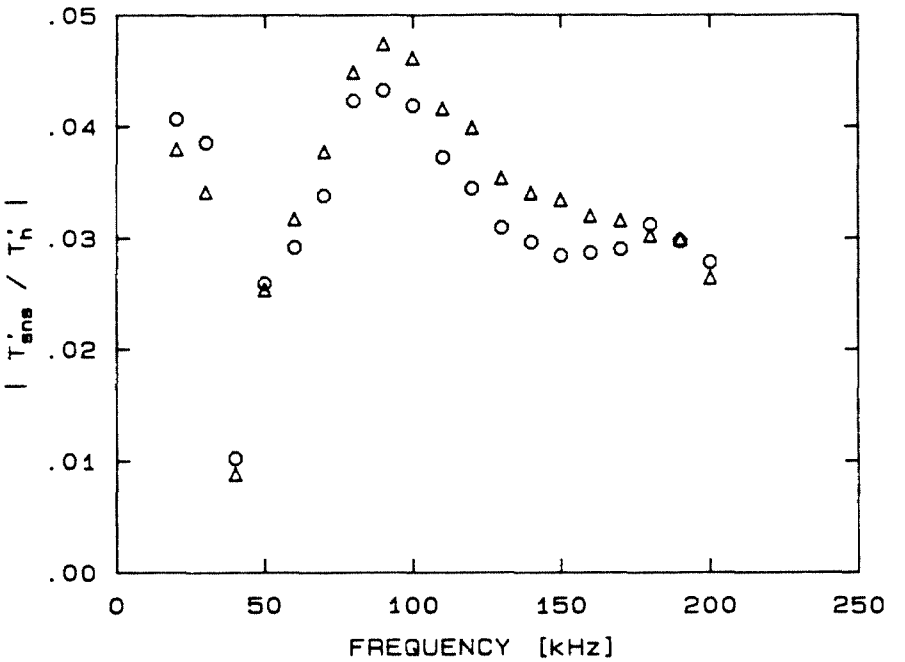

Figure 4.7. Test of the scattering response as function of the incident wave amplitude. The family of data points plotted with symbol Δ has twice the incident amplitude compared to the other (O) set.

A very simple test can be performed to check whether the sensor measures scattered waves or other signals, for example diffracted waves from the heater. Figure 4.8 shows the results of the frequency sweeps for a 0.001" thick wire and the empty cavity under otherwise identical conditions. The frequencies cover the range from 20 kHz to 205 kHz in 5 kHz steps; the heater temperature is again 85 μK. Clearly, the signals received with the target in the focal point are much stronger and qualitatively different. Thus, the observed signatures are by

definition scattered wave components. This evidence is supported by the close match between the theoretically calculated and measured arrival times in the cavity. Furthermore, scattering signals may also be observed when the heater pulse passes through the target area for the second time, that is after reflection from the sensor backside (see Figure 2.3). This is a geometrically different situation compared to the first passage and leads to the conclusion that diffracted waves directly from the heater are not being measured (except, maybe, for the little "tail" visible in Figure 4.8 at low frequencies).

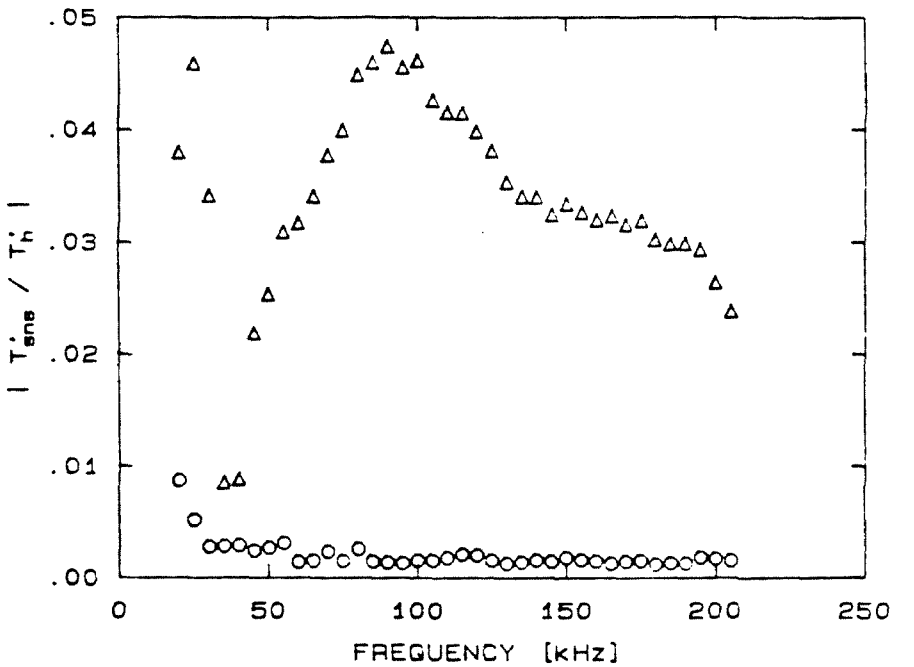

Figure 4.8. Comparison of the scattering signature of a wire (Δ) with the no-target (O) case.

Finally, we present the results for two different cylinder radii. The first case is again the .001" diameter wire, which is now compared with the scattering signature of a .0005" target. As in the previous example, 38 frequencies between 20 kHz and 205 kHz are used, with a 85 μK temperature perturbation T_h' at the heater. Both results, when plotted as a function of the dimensionless

wavenumber ka, should collapse on the same curve. Figure 4.9 displays the data in that fashion, and the agreement is good only in a small region around $ka \approx 0.2$. The theoretical estimate derived in Chapter 3 is also displayed as the continuous curve. It predicts roughly the correct order of magnitude of the signal, but the region of agreement with the data is limited. One has to keep in mind that the model used in Chapter 3 to derive the signal estimate makes simplifying assumptions for the wave propagation in the cavity.

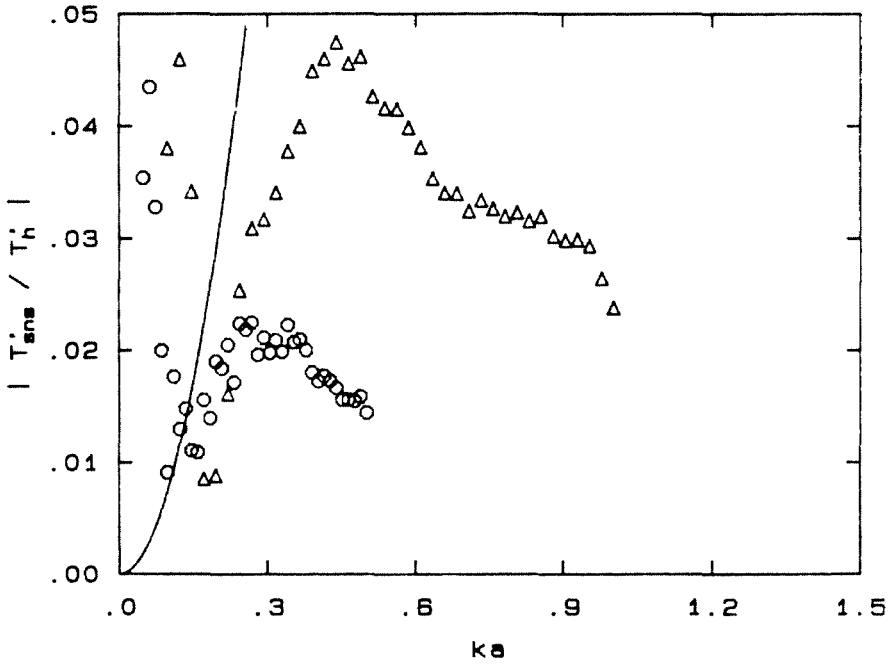

Figure 4.9. Comparison of the scattering from a 0.001" wire (Δ) and a 0.0005" target (O). The solid line is the theoretical result derived in Chapter 3.

The explanation for the increase in the observed signals at very low frequencies (wavenumbers) lies probably in the appearance of cavity-dependent diffraction effects. Two observations point in this direction. First, the no-target case, which has been presented in Figure 4.8, shows some signals at the corresponding frequencies. If one plots the results of Figure 4.9 as a function of

frequency, not wavenumber ka, the two low frequency tails are almost identical. This clearly excludes any influence of the wire targets, because they must scale with their respective radii, or thus ka.

The drop of the scattering response at high frequencies compared to the theory cannot be explained by low frequency diffraction phenomena. Since the data have been corrected for the influence of second sound attenuation, this effect is eliminated, too. Most likely, the cause of the amplitude loss is target misalignment. In Chapter 2, some plots were shown for the relative size of the target wire and the focal area as defined by the spatial selectivity (Figures 2.4a - 2.4e). If one assumes a displacement of the target out of the center of the focal area, the observed scattering signal will of course decrease. This drop becomes more pronounced with increasing frequency or decreasing size of the focal area. The relative position accuracy required is always a few wavelengths. For high frequencies, this means alignment to within a few thousands of an inch. With the present cavity design, such precision positioning is not possible and the appearance of an artificial drop in the scattering amplitude can be expected.

We now summarize the results obtained from the wire scattering experiments in the double elliptical cavity:

- The concept of focused second sound waves in a reflecting cavity can be used to study scattering phenomena.

- For the case of a wire target, the observed scattering signatures agree reasonably well with the theory, as far as signal strength is concerned.

- Low frequency diffraction effects and alignment requirements restrict the wavenumber range over which self-similar scattering can be observed.

— The medium resistance sensor can be used in connection with signal averaging to detect temperature fluctuations in the μK regime.

Chapter 5

THE PARABOLIC CAVITY

In the second part of the thesis we will describe two experiments which involve scattering of second sound from fluid motion. Since the elliptical cavity did not seem sensitive and versatile enough for this purpose, a new experimental cell was developed.

5.1. Principle of Operation and Geometry

The necessary increase in sensitivity is achieved in two ways. First, the design was changed to provide a larger angle over which the scattering signal is observed. In addition, it was decided to use very large resistance sensors, which have a better signal output for a given dissipation rate. Both constraints finally led to a configuration based on parabolic reflectors instead of ellipses. Consider Figure 5.1, which shows an off-axis section of a parabola. A cylindrical wave emerging from the focus F will be converted into a plane wave upon reflection from the sidewall. A sensor placed at the end of the reflector can integrate this plane wave over a large area, corresponding to a wide solid angle of the original cylinder wave.

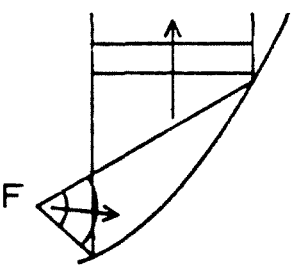

Figure 5.1. Basic operation of an off-axis parabolic reflector (see text).

There is one problem with this approach, however, which makes it less useful for the generation of a cylindrical *incident* wave to probe the focal region. If one assumes a uniform amplitude distribution in the wave generated at the sensor/heater surface, the reflected wave will no longer have that uniformity, now as a function of the polar angle. Since a second sound wave produced by a dissipative heater always includes a DC counterflow component, this would translate into an undesirable shear flow component in the focus. The problem is also present in the elliptical cavity, but the half axis ratio of 0.9 makes the effect in that case much less pronounced.

The final cavity design, depicted in Figure 5.2, avoids the problem by using a cylindrical section for the heater H and three confocal parabolas for the forward (S_1) and sidelooking sensors (S_2,S_3). Constraints on the overall cavity size forced the heater to be focused on a virtual focus P. One of the straight sidewalls acts as a mirror to map this point onto the true focus F.

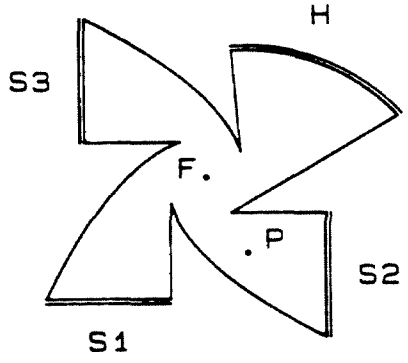

Figure 5.2. Schematic of the parabolic cavity.

The incident wave passes through the focal area and is received by sensor S_1. If there is no disturbance in the focus, the other two sensors will not register this wave, except of course for some weak diffracted components originating for example at the four corners close to the center. It should be pointed out that

the diffracted wavefronts are not matched to the sensor surfaces and thus will not create a full signal. On the other hand, a scatterer which produces cylindrical waves emerging from the cavity center is readily "seen" by the side sensors. The forward sensor can provide accurate timing information for the other two because of the equal pathlengths. The asymmetry of the cavity ensures that the diffracted waves received by S_2 and S_3 are not equal and can be distinguished from the strongly correlated scattering signatures. The sidewall sensors cover an angle of 78.95^0 each. Figure 5.3 displays the overall sensitivity pattern as computed from the diffraction pattern of the heater and one of the sensors. The scaling and spacing of contour values is the same as in the case of the elliptical geometry.

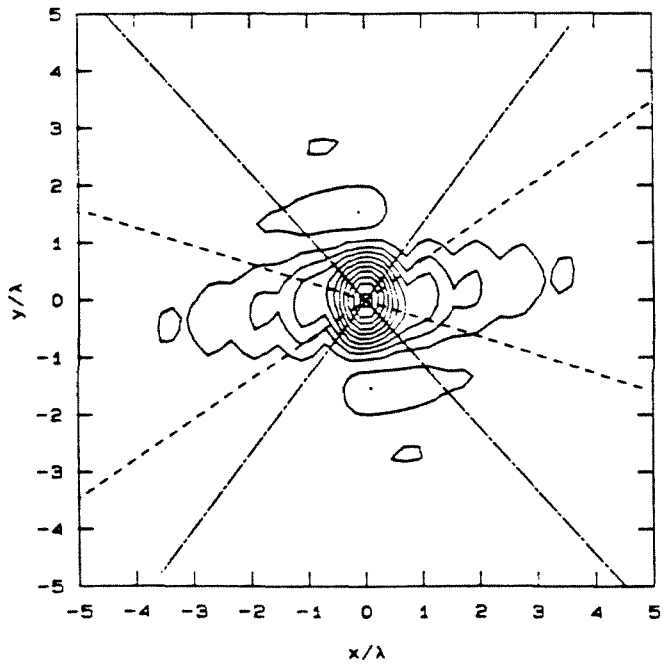

Figure 5.3. Sensitivity pattern of the parabolic cavity.

Again, the cavity is machined out of a brass block using the numerically controlled milling machine (see Appendix A). In this case, the depth of the profile is only 0.1" compared to the 0.5" of the ellipses. The equation for the parabolic side faces is

$$y = 1.18347\,x^2 - 0.21124$$

where x and y are the absolute coordinates in inches. The width of the sensor windows is .665", whereas the heater covers an angle of 52.39 degrees. Sensors and heater are clamped to the straight side faces formed by the cavity and a matching cover plate. A thin (0.005") Teflon sheet insulates their metallic surfaces from the cavity.

5.2. Heaters and Sensors

The heater substrate is a section of precision bore glass tubing (Wilmad Glass Co., New Jersey) of 0.095" thickness and an inner radius of 1.08925", with at most ± 0.0004" deviation. This radius is closely matched to the radius of the cavity at helium temperatures. This matching, in connection with the Teflon sheet, provides adequate sealing, although superleaks probably still exist. A Nichrome thin film is deposited on the glass surface using a rotating vacuum deposition stage. This assures a uniform film thickness and consequently a uniform wave strength. The film pattern is created by a photolithographic method ("Liftoff"), which will be discussed in more detail for the sensors. One distinguishing feature should be mentioned, though. Instead of the usual high resolution photographic plates, a flexible plastic film was used during the exposure of the photosensitive coating. In this way, the heater pattern was contact printed directly onto the curved surface. The electrical connection is made by two copper thin film pads at the ends of the Nichrome film. The actual resistance values for the heater varied - the one used in all the experiments discussed later

has 425 Ω .

The forward sensor is a simple granular aluminum film with the transition temperature raised by admission of oxygen during the evaporation. No scribing is performed to increase the sensitivity, since the transmitted incident wave can easily be recorded. Usual normal resistances are around 50 Ω , thus providing a good impedance match to the coaxial cables leading to the outside of the dewar.

The sidelooking sensors are designed for very large resistances. In order to form a line pattern in the thin film surface, photolithography with 4 μm feature size is used. The steps involved in the mask making and pattern generation are desribed in Appendix E. With a special redundancy feature, the typical sensor has a resistance between 1 and 3 MΩ , depending on the number of faults in the film pattern and the amount of oxidation. It covers an area of .09" × .665" and has an "aspect ratio," that is the ratio length/width, of about 600,000.

At this point we will take a closer look at the benefits of improving the sensor resistance. Thinking in terms of the active sensor area A, the resistance and thus the sensitivity S increase roughly as

$$S \propto A .$$

If a cylindrical wave is received, its amplitude T decays with the square root of the observation distance L and since $A \propto L$ for a constant angle subtended by the sensor,

$$T \propto A^{-\frac{1}{2}} .$$

The sensor signal V, which is the product of the sensitivity and the wave

amplitude, becomes

$$V = S \times T \propto A^{\frac{1}{2}}.$$

The relevant quantity is of course the signal-to-noise ratio. Assuming for simplicity that the major contribution is thermal (Johnson) noise from the sensor, the rms noise voltage N is proportional to the square root of the sensor resistance, or

$$N \propto A^{\frac{1}{2}}$$

so that finally

$$\frac{V}{N} = const.$$

This would indicate that an increase in sensor resistance will not improve the effective performance of the detection system. However, one has to take into account the noise added during the amplification of the sensor signal. Its contribution to the total noise should be kept as small as possible. Only large sensor resistances will increase the detector noise (and, of course, the signal) to the point where the amplifier noise becomes negligible.

This leads to new complications. The coaxial cables, which transfer the sensor signal to the outside of the dewar, have an intrinsic capacitance. If no special measures are taken, the original sensor signal can be attenuated by several orders of magnitude due to capacitive loading. A simple emitter-follower circuit placed close to the sensor can solve this problem. Appendix B describes some aspects of such a design. Figure 5.4 gives a schematic representation of the

electronics associated with each of the side sensors. A field-effect transistor (MOSFET), which can operate at cryogenic temperatures (see Appendix F), serves as the driving amplifier. Although it can work fully submerged in the helium bath, the best performance is achieved when it is above the liquid level, that is in the cold helium vapor.

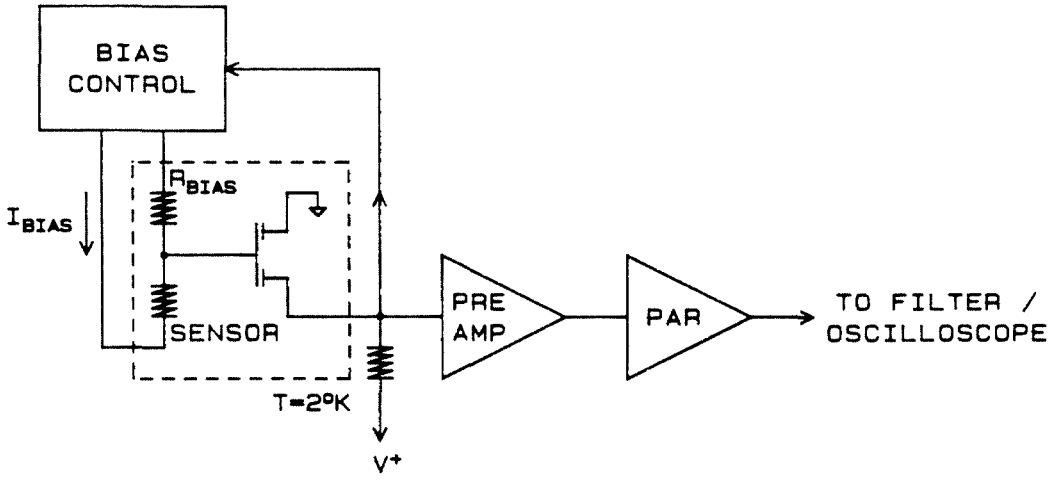

Figure 5.4. Schematic of the high-impedance sensor electronics.

For noise considerations, the sensor biasing resistor is placed in the low temperature part of the circuit, too. The sensor is DC coupled to the transistor gate, thus avoiding extra low temperature components for the biasing network. The bias current for the sensor is generated by an integrated current source, usually set to about 20 μA. The operating point of the MOSFET is fixed by a feedback circuit which is incorporated in the sensor biasing electronics to provide the proper gate offset voltage. The sensor signals are conducted through miniature coaxial cables to the outside amplifiers. In addition, the cables themselves are fed through a thin stainless steel tube, which serves as a second noise shield. Similarly, the experiment is wrapped in a superconducting shield made from tantalum foil. Attached to the dewar top is a first amplifier stage, which uses an ultra low-noise discrete transistor (Teledyne Crystalonics 2N6550) to

keep the additive noise contributions low. For further amplification, a standard amplifier (Princeton Applied Research PAR 113) was chosen.

Photo 5.5 shows the parabolic cavity partially disassembled to render the various components visible. The double s-shaped pattern on one of the cavity pieces is an additional heater which is positioned right in the focal point. It is used for calibration of the side sensors and as a flow generator for one of the scattering experiments.

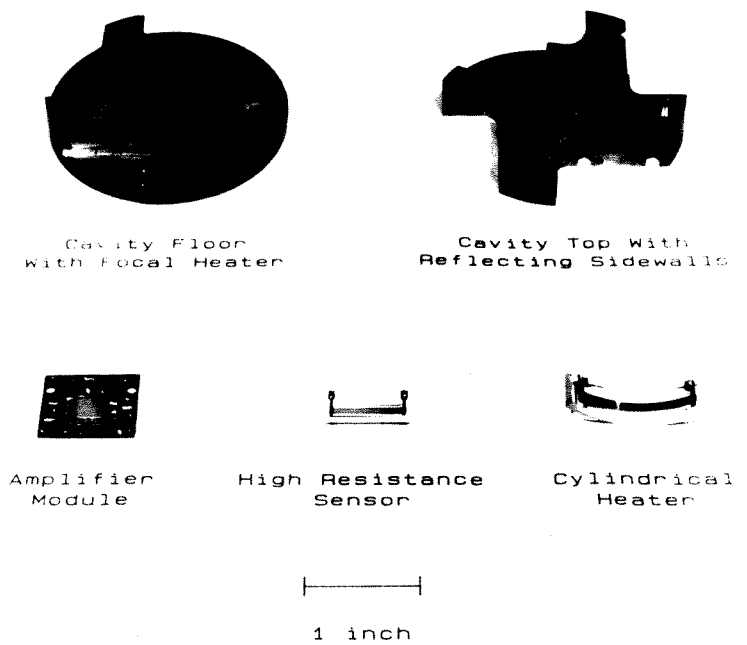

Figure 5.5. Photograph of the parabolic cavity.

Again, the heater is formed by a Nichrome thin film, here with dimensions 100 μm by 100 μm. Contact is made by two indium films which are seen in the photo as the double s-shaped pattern. Since indium is a superconductor, the contacts operate without dissipation and do not disturb the waves propagating in that

part of the cavity. Superconducting wires are bonded with conductive epoxy resin to the film leads and connect the heater to a coaxial cable. The resistance of this heater is 28 Ω. Photo 5.6 is a microscope picture of the central Nichrome film, with the leads being visible as the large adjacent structures. Since the cavity itself is conducting, an adequate insulation has to be provided. Early attempts with a silicon monoxide layer failed because of the presence of small pinholes shorting out the heater current path. The surfaces of both cavity halves were finally lapped with a 5 μm compound to remove tool marks and small scratches. A thick layer of polyimide plastic (see Appendix E) is then deposited to generate a flat, insulating substrate layer. The metal films are vacuum-deposited using a metal mask to accurately align the cavity piece. The dimensions of the center area are in addition controlled by photoresist patterns and liftoff processing. The second cavity piece has two shallow (0.0005") grooves cut into the surface where the heater leads would touch otherwise. A final benefit of the polishing and coating is the improved sealing between the two cavity halves.

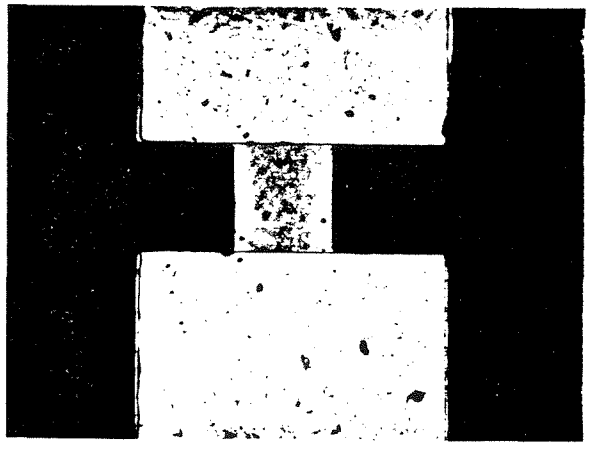

Figure 5.6. The central heater as seen under the microscope. The magnification is 200×.

Chapter 6

EXPERIMENTAL RESULTS

We proceed now with the discussion of the calibration results for the three cavity sensors. In addition, a scattering experiment will be described in which the central heater element is used as a source of fluid disturbances.

6.1. Sensor Calibration

The forward sensor (S_1) serves as a reference for the other two because of its conventional design and low resistance. Figure 6.1 shows a standard calibration curve for S_1, obtained by slowly varying the saturated vapor pressure and thus the temperature over the helium bath.

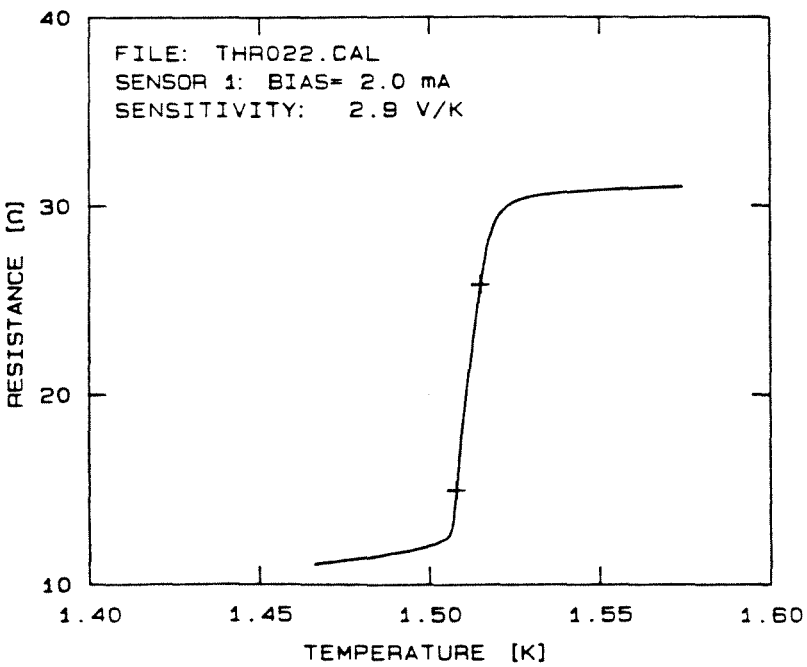

Figure 6.1. Calibration curve of the forward sensor.

The normal resistance value of about 30 Ω guarantees that no capacitive

loading will affect the signal output. The transition curve was used to determine a temperature sensitivity of 2.9 V/K by fitting a straight line to the data between the two endpoints indicated in the plot.

Figure 6.2 shows the calibration curves measured for the side sensors S_2 and S_3. Due to their higher resistance and the necessary biasing networks (see Figure 5.4), the measurements are somewhat more elaborate. One may notice that the resistance of the sensors at the superconducting end of the transition is finite.

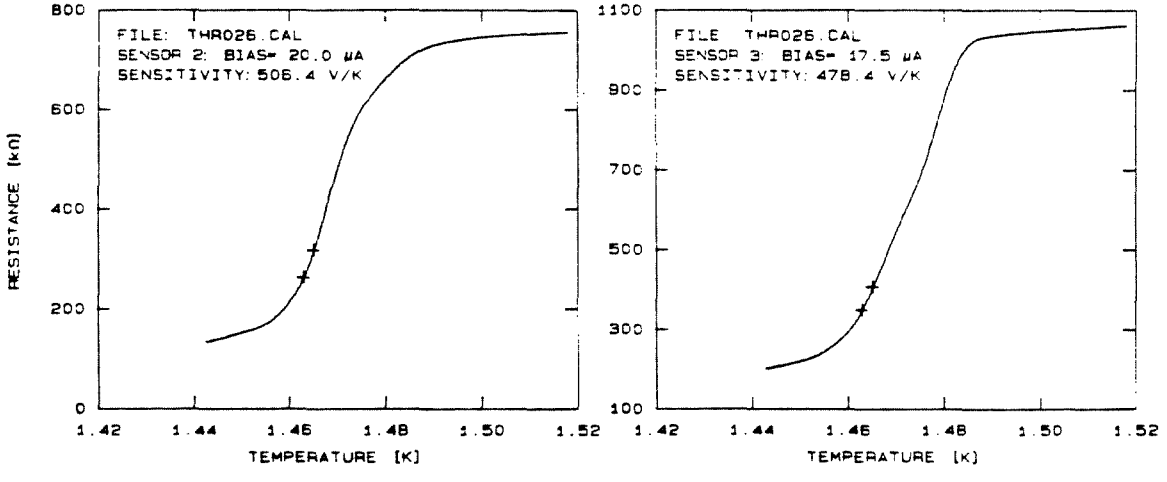

Figure 6.2. Calibration curves of the side sensors S_2 and S_3.

This is most likely an artefact introduced by offset errors in the various monitoring amplifiers and by a shift in the resistance of the bias resistors, which are inaccessible during the calibration runs. At any rate, the calculation of the temperature sensitivity should not be affected by this, since it depends only on the slope of the data. A more interesting fact is the difference in the transition

temperature between the side sensors and the forward element. Two effects are the most likely explanation for this. During the film evaporation, the forward sensor surface was positioned slightly farther away from the evaporation source than the other two sensor substrates. The resulting film thickness d is somewhat smaller, and for the absolute values involved ($d \approx 2.5\times10^{-8}$ m), this may cause a shift in the transition temperature. The general trend is in the right direction, as a decrease in film thickness is known to push up the transition temperature [1]. Secondly, one has to look at the current densities present in the two sensor types during operation. The forward sensor with a width W of .15" and a current I_0 of 2 mA gives a value

$$\rho_c = \frac{I_0}{W} = 0.52 \ \frac{\mathrm{A}}{\mathrm{m}},$$

whereas for the side sensors with $I_0 \approx 10\ \mu$A and $W \approx 4\ \mu$m, the number is

$$\rho_c \approx 2.5 \ \frac{\mathrm{A}}{\mathrm{m}}.$$

The effective bias current for the side sensors is about half the externally applied value because of the bypass that is provided for (almost) every loop in the sensor pattern. The current density is thus a factor of 5 higher in the high resistance sensors, an effect which will shift their transition point.

The particular set of sensors had fairly low transition temperatures (1.46 K and 1.51 K). The sensitivities achieved by the side sensors (S_2: 506 V/K, S_3: 478 V/K) are linked to the transition characteristics because of the film material used. Pure aluminum becomes superconducting at T=1.18 K. The transition point is moved up by introducing oxygen during the evaporation. The formation of oxidized granules leads to an increase in the specific sensor resistance.

Consequently, enforcing higher transition temperatures results in higher impedance sensors and larger sensitivities. For several sensors with resistances of about 2 MΩ, sensitivities in excess of 1000 V/K were obtained.

The calibration curves described so far were measured with very slowly changing temperatures. The sensitivities calculated might thus not represent the actual values for operation at high second sound frequencies. Thermal and especially electronic capacitances will probably degrade those figures. In order to avoid the problem, a dynamic calibration was performed in the cavity using the central heater element. A second sound burst is emitted from the focal heater and received by all three sensors. The heater points upwards in the cavity and will not produce a "clean" cylindrical wave. An absolute calibration referenced to the heater input signal is thus not possible. However, the cavity geometry is such that all sensors will record the same signal, independent of its actual history of generation. The forward sensor is used to establish a reference for the other two devices. Figure 6.3 shows a typical second sound burst as received by the forward sensor at T=1.51 K. Here, the sensitivity derived from the data of Figure 6.1 was used to compute the effective temperature excursion. The displayed trace is an average over 200 individual bursts. The heater signal which generated this pulse was a 50 kHz, 140 μs burst of 227 mV peak-to-peak amplitude. Using a heater area A of 100 μm × 100 μm, a resistance R of 26 Ω and the appropriate values for the helium density ρ, specific heat c and second sound velocity a_2, the temperature fluctuations at the heater surface become

$$T' = \frac{V_{pp}^2}{8RA\rho a_2 c} \approx 7.15 \text{ mK} .$$

One sees immediately that the heater is not a very effective wave generator in the specific cavity geometry, because the received amplitude is much smaller

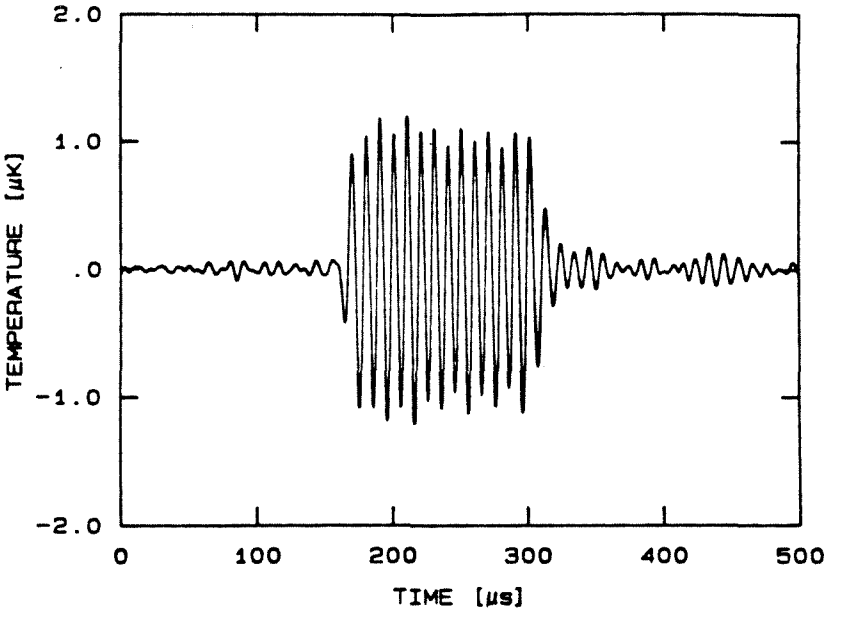

Figure 6.3. Typical calibration waveform generated in the focus and received by the forward sensor.

than what would be predicted based on a simple outgoing cylindrical wave. The modulation of the signal visible in Figure 6.3 is not a consequence of nonlinear wave propagation, but due to a residual DC offset in the pulse driving the heater.

This signal can now be compared to the ones received from S_2 and S_3, which are shown in Figure 6.4 at T=1.46 K. The data are plotted as voltages here, since the effective sensitivity is the unknown conversion factor. Postulating that the average signal strength is the same for all three sensors, the sensitivities become 303.9 V/K for S_2 and 159.8 V/K for S_3. These numbers were computed using average amplitudes determined by the algorithm introduced in Chapter 3. The numerical values are lower than the ones measured with the "DC-calibration" method discussed earlier. They also change with the frequency used in the calibration scheme (in the example above, f = 100 kHz). The most likely cause for this is a hidden thermal time constant in the sensors. Measurements

of the electrical characteristics of the sensors did not show any significant capacitances. The residual input capacitance of the first stage amplifiers were already incorporated in an effective gain. On the other hand, similar reductions in the effective sensitivity were observed for second sound shock measurements in a different experimental set-up.

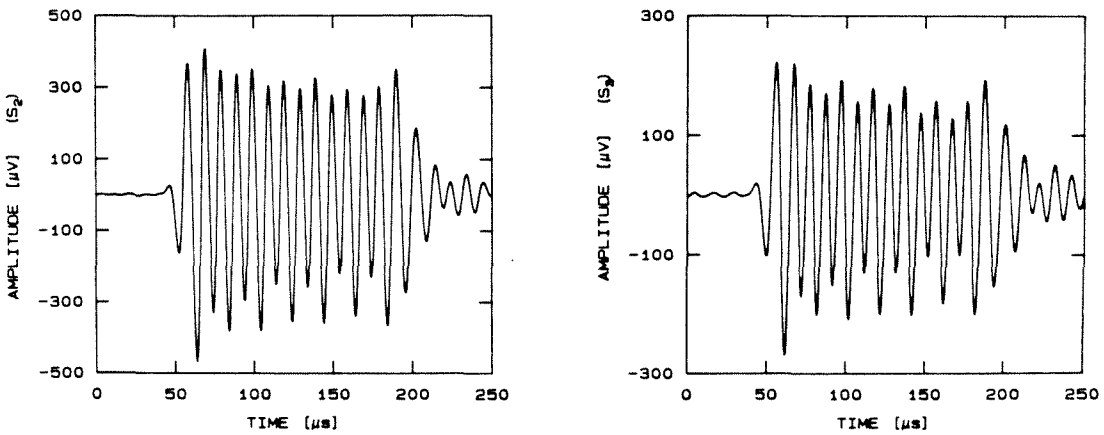

Figure 6.4. The same waveform as in Figure 6.3, seen by S_2 and S_3.

6.2. Scattering from Fluid Disturbances

In a second mode of operation, the central heater is used as a source of flow disturbances in the helium. By passing a DC current through the heater, a counterflow is set up in the vicinity of the focal point. If the induced flow velocities are high enough, turbulence will be generated and eventually fill the cavity. A second sound wave passing undisturbed through the focal area will not be recorded by the side sensors. The turbulence, however, will scatter the incident wave and in this case a signal should be received. The cavity sensitivity pattern

(Figure 5.2) selects only a small region near the focus from which the scattering will be registered. In the experiment described next, the main (cylindrical) heater was pulsed so as to produce the probing second sound wave. Here, a 80 kHz sinusoidal burst of 140 μs duration was used. The temperature excursion produced at the heater surface was

$$T_h' = 132\ \mu\mathrm{K},$$

from which an estimate for the strength of the incident wave in the focus can be derived. Using the representation of a cylindrical wave introduced in Chapter 3, the amplitude becomes for a heater of half-angle ψ_0, focal length r_0, frequency f and second sound velocity a_2

$$T_f' = 2\,\psi_0 \left(\frac{k r_0}{2\pi} \right)^{\frac{1}{2}} T_h' = 2\,\psi_0 \left(\frac{r_0 f}{a_2} \right)^{\frac{1}{2}} T_h' \approx 1.27\ \mathrm{mK}\ .$$

Figure 6.5 shows the signals received and averaged (200 realizations) by the side sensors with the central heater *not* in operation. No correlation between the two channels can be observed and the overall signal level, as defined by the rms-value computed from the average, is about 10.9 nK for S_2 and 22.4 nK for S_3. The dynamic sensitivities of the sensors at f = 80 kHz were measured with the scheme described above and used to calculate the effective temperature excursions.

For the results displayed in Figure 6.6, the same incident wave was used. As a difference, though, the central heater dissipated a 14.3 mA DC current. A strongly correlated signal can be seen on both side sensors, representing the scattered incident wave. It should be stressed again that the flow induced by the central heater does not contain in itself a signal like the one observed. The only

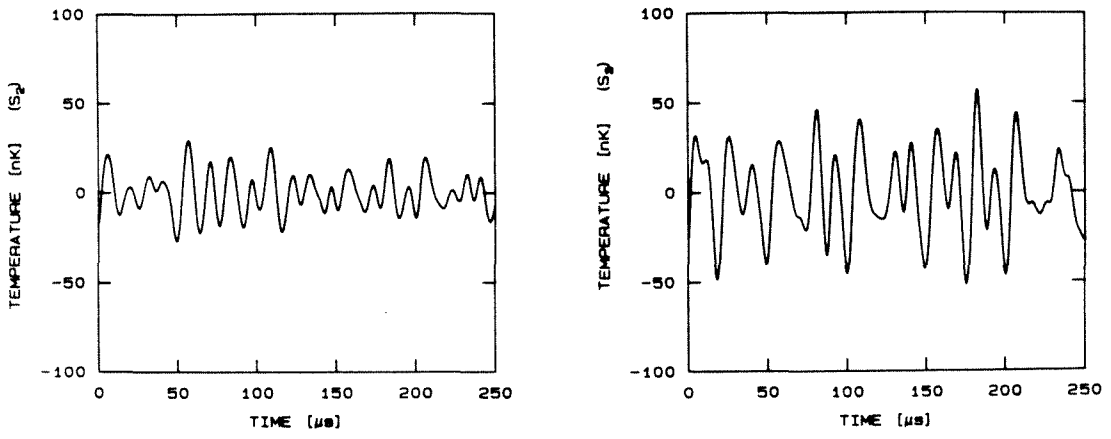

Figure 6.5. Waveforms without scattering from the focal region.

effect noticeable without a probing incident wave is a general increase in the noise detected by the sensors. This is indicative of the turbulent character of the flow induced in the focus. A rough estimate for the heat flux in the focal point gives a value of $Q \approx 53$ W cm^{-2}. At this rate of dissipation, boiling of the helium has been observed in second sound shock experiments [2]. Such an effect would of course produce a strong source of scattering. However, signals similar to the ones shown above were also recorded for much smaller heat fluxes (10 W cm^{-2}), where boiling should not be a problem. In addition, the true heat fluxes are probably much lower, since the conduction loss into the cavity body, which was neglected in the estimate for Q, becomes important for steady-state operation of the heater.

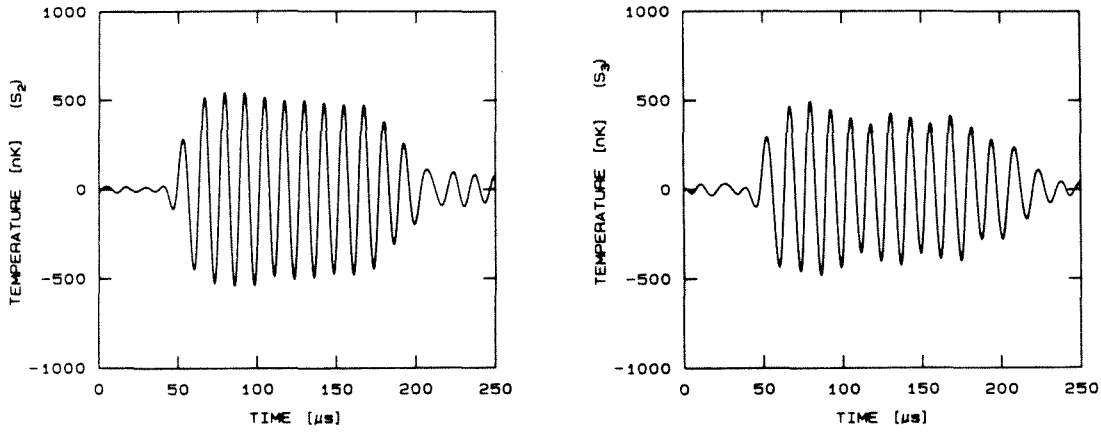

Figure 6.6. Waveforms due to scattering from counterflow in the focal region.

6.3. References

1. Maissel, L. and Glang, R., *Handbook of Thin Film Technology*, McGraw-Hill, New York (1970), Chapter 22.

2. Gerthsen, D., Torczynski,J. and Rösgen,T., submitted to Phys. Fluids .

Chapter 7

SECOND SOUND SCATTERING FROM A VORTEX LINE

In this chapter we will consider the scattering of second sound from quantized vortex lines in rotating superfluid helium. A theoretical derivation is presented first in order to provide an estimate for the magnitude of the effect. A short introduction to quantized vortex lines is given in appendix C, and we will use certain results stated there without further justification. This part is followed by the presentation of some results obtained with the parabolic cavity mounted in a rotating dewar.

7.1. A Theoretical Estimate for the Scattering

The interaction of normal sound waves with vortices has already been studied by many investigators [1-9]. In some publications, the same ideas were also applied to quantized vortex lines in liquid helium [10,11]. It seems, however, that only first sound was considered as an incident wave. Thus, the results turn out to be completely equivalent to the normal acoustic case, except, of course, for the quantization of circulation. On the other hand, second sound scattering will prove to be slightly different, not only because of the comparatively small speed of wave propagation.

Since the present experiment works in a rotating frame of reference, one should include the appropriate rotation terms in the equations. The Rossby number of the problem appears to be large enough, though, to allow omission of those terms. We will use the two-fluid equations, ignoring also dissipative and mutual friction terms.

The following notation will be used:

ρ = total density , ρ_s = superfluid density , ρ_n = normal fluid density,

$\vec{v}$ = bulk velocity , $\vec{w}$ = counterflow velocity,

$\vec{v}_n$ = normal fluid velocity , $\vec{v}_s$ = superfluid velocity,

p = pressure , T = temperature , s = specific entropy

The two fluid model with the assumptions described above leads to the following set of equations:

$$\rho = \rho_s + \rho_n \tag{7.1}$$

$$\rho\vec{v} = \rho_s\vec{v}_s + \rho_n\vec{v}_n \tag{7.2}$$

$$\vec{w} = \vec{v}_n - \vec{v}_s \tag{7.3}$$

$$\frac{\partial\rho}{\partial t} + \nabla \cdot \left[\rho\vec{v} \right] = 0 \tag{7.4}$$

$$\frac{\partial}{\partial t}\left[\rho\vec{v} \right] + \nabla \cdot \left[\rho\vec{v}\vec{v} + \frac{\rho_s\rho_n}{\rho}\vec{w}\vec{w} + pI \right] = 0 \tag{7.5}$$

$$\frac{\partial}{\partial t}\left[\vec{v}_s \right] + \frac{1}{\rho}\nabla p - s\nabla T - \frac{1}{2}\frac{\rho_n}{\rho}\nabla\left[w^2 \right] + \frac{1}{2}\nabla\left[{v_s}^2 \right] = 0 \tag{7.6}$$

$$\frac{\partial}{\partial t}\left[\rho s\right] + \nabla\cdot\left[\rho s\vec{v}_n\right] = 0\,. \tag{7.7}$$

We introduce a cylindrical polar coordinate system (r, θ, z) and assume a vortex line located at the origin, parallel to the z axis. An arbitrary quantity of the flow field, say $a(\vec{r},t)$, will be split up into an ambient part a_0, a part due to the vortex motion $\bar{a}(\vec{r})$, and a component associated with the second sound wave field, $a'(\vec{r},t)$.

$$a(\vec{r},t) = a_0 + \bar{a}(\vec{r}) + a'(\vec{r},t)\,. \tag{7.8}$$

The vortex line is characterized by a steady superfluid velocity field $\vec{v}_s(\vec{r})$ and the corresponding pressure term $\bar{p}(\vec{r})$. All the other quantities, especially density, entropy, and temperature will be assumed to stay unchanged due to the vortex flow.

The second sound wave present in the flow introduces temperature or entropy fluctuations $T'(\vec{r},t)$, $s'(\vec{r},t)$, as well as a counterflow velocity $\vec{w}'(\vec{r},t)$. In agreement with the linearized theory of sound propagation in helium, we assume that the total density ρ , the pressure p and the bulk velocity $\vec{v}$ are not perturbed by second sound.

Thus the flow quantities can be written in notation (7.8):

$$\rho = \rho_0,\quad \rho_s = \rho_{s_0} + \rho_s',\quad \rho_n = \rho_{n_0} + \rho_n'$$

$$\vec{v} = \bar{\vec{v}},\quad \vec{w} = \bar{\vec{w}} + \vec{w}'$$

$$\vec{v}_n = \vec{v}'_n, \quad \vec{v}_s = \vec{\bar{v}}_s + \vec{v}'_s,$$

$$p = p_0 + \bar{p}, \quad T = T_0 + T', \quad s = s_0 + s' .$$

Now, all perturbations are assumed to be sufficiently small to permit the linearization of equations (7.1) - (7.7). We will neglect all terms containing products of two wave quantities (for example $\rho_s'\vec{v}'_s$). These terms eventually lead to frequency doubling and will not contribute to the scattering at the frequency of the incident wave. However, terms consisting of a vortex and a wave quantity (e.g., $\rho_s'\vec{\bar{v}}_s$) will be retained - they represent the coupling between the wave motion and the vortex. All products with more than two non-constant quantities will be dropped, too.

With these assumptions, equation (7.7) becomes

$$\rho_0 \frac{\partial s'}{\partial t} + \rho_0 s_0 \nabla \cdot \vec{v}'_n = 0 . \tag{7.9}$$

Taking the time derivative of this equation and dividing by ρ_0 gives

$$\frac{\partial^2 s'}{\partial t^2} + s_0 \nabla \cdot \left(\frac{\partial \vec{v}'_n}{\partial t} \right) = 0 . \tag{7.10}$$

Using equation (7.2) , the normal velocity can be linked to the superfluid velocity, since $\vec{v} \equiv 0$ is assumed:

$$\frac{\partial \vec{v}'_n}{\partial t} = - \frac{\rho_{s_0}}{\rho_{n_0}} \frac{\partial \vec{v}'_s}{\partial t} - \frac{1}{\rho_{n_0}} \vec{\bar{v}}_s \frac{\partial \rho_s'}{\partial t} . \tag{7.11}$$

Equation (7.6) becomes upon linearization

$$\frac{\partial \vec{v}'_s}{\partial t} = -\frac{1}{\rho_0} \nabla \bar{p} + s_0 \nabla T' \tag{7.12}$$

$$+ \frac{1}{2} \frac{\rho_{n_0}}{\rho_0} \nabla \left(\vec{w}^2 + 2 \vec{w} \cdot \vec{w}' \right) - \frac{1}{2} \nabla \left(\vec{v}_s^2 + 2 \vec{v}_s \cdot \vec{v}'_s \right) .$$

The counterflow velocity can be replaced using equation (7.3) :

$$\vec{w} = -\vec{v}_s \tag{7.13a}$$

$$\vec{w}' = -\frac{\rho_0}{\rho_{n_0}} \vec{v}'_s . \tag{7.13b}$$

Substituting (7.13) into (7.12) and dropping higher order terms gives:

$$\frac{\partial \vec{v}'_s}{\partial t} = -\frac{1}{\rho_0} \nabla \bar{p} + s_0 \nabla T' - \frac{1}{2} \frac{\rho_{s_0}}{\rho_0} \nabla \left(\vec{v}_s^2 \right) . \tag{7.14}$$

Similarly, equation (7.5) can be written as

$$0 = \nabla \bar{p} + \rho_{s_0} \nabla \cdot \left(\vec{v}_s \vec{v}_s \right) + \rho_{s_0} \nabla \cdot \left(\vec{v}_s \vec{v}'_s + \vec{v}'_s \vec{v}_s \right) . \tag{7.15}$$

The pressure term in (7.14) is eliminated by using (7.15)

$$\frac{\partial \vec{v}'_s}{\partial t} = \frac{\rho_{s_0}}{\rho_0}\left[\nabla \cdot \left(\vec{v}_s \vec{v}_s \right) - \frac{1}{2} \nabla \left(\vec{v}_s^{\,2} \right) + \nabla \cdot \left(\vec{v}_s \vec{v}'_s + \vec{v}'_s \vec{v}_s \right) \right] + s_0 \nabla T' . \quad (7.16)$$

The vortex flow is assumed to be divergence-free ($\nabla \cdot \vec{v}_s \equiv 0$), and irrotational ($\nabla \times \vec{v}_s \equiv 0$). In this case, a vector identity holds:

$$\nabla \cdot \left(\vec{v}_s \vec{v}_s \right) = \left(\vec{v}_s \cdot \nabla \right) \vec{v}_s = \frac{1}{2} \nabla \left(\vec{v}_s^{\,2} \right) .$$

Using this identity in equation (7.16) and substituting the result back into (7.11) gives

$$\frac{\partial \vec{v}_n'}{\partial t} = - \frac{\rho_{s_0}}{\rho_{n_0}} s_0 \nabla T' - \frac{\rho_{s_0}^{\,2}}{\rho_0 \rho_{n_0}} \nabla \cdot \left(\vec{v}_s \vec{v}'_s + \vec{v}'_s \vec{v}_s \right) - \frac{1}{\rho_{n_0}} \vec{v}_s \frac{\partial \rho_s'}{\partial t} . \quad (7.17)$$

This equation can be used to replace the normal fluid velocity term in equation (7.10)

$$\frac{\partial^2 s'}{\partial t^2} - \frac{\rho_{s_0}}{\rho_{n_0}} s_0^{\,2} \nabla^2 T' = \quad (7.18)$$

$$\frac{s_0}{\rho_{n_0}} \vec{v}_s \cdot \nabla \frac{\partial \rho_s'}{\partial t} + \frac{\rho_{s_0}^{\,2}}{\rho_0 \rho_{n_0}} s_0 \nabla \cdot \left[\nabla \cdot \left(\vec{v}_s \vec{v}'_s + \vec{v}'_s \vec{v}_s \right) \right] .$$

Since there are no pressure perturbations in the problem, we can use the following thermodynamic identity to replace the entropy in (7.18):

$$ds = \left.\frac{\partial s}{\partial T}\right|_{p,w^2} dT = \frac{c}{T}\, dT \tag{7.19}$$

where c is the specific heat of helium.

Thus we finally obtain

$$\frac{\partial^2 T'}{\partial t^2} - a_2^2\, \nabla^2\, T' = \tag{7.20}$$

$$\frac{s_0 T_0}{c \rho_{n_0}} \left\{ \vec{v}_s \cdot \nabla \left(\frac{\partial \rho_s'}{\partial t} \right) + \frac{{\rho_s}_0^2}{\rho_0} \nabla \cdot \left[\nabla \cdot \left(\vec{v}_s \vec{v}'_s + \vec{v}'_s \vec{v}_s \right) \right] \right\}$$

Here, the definition for the speed of second sound was used:

$$a_2^2 = \frac{\rho_{s_0}}{\rho_{n_0}} \frac{{s_0}^2 T_0}{c}. \tag{7.21}$$

We will now drop the subscripts for the ambient values of the variables to simplify the notation. Also, all fluctuating quantities are assumed to have an $e^{-i\omega t}$ time dependence. Here ω denotes the frequency of the incident wave.

The time derivative of the superfluid density can be approximately replaced by

$$\frac{\partial \rho_s'}{\partial t} \approx \left.\frac{\partial \rho_s}{\partial T}\right|_{p,w^2} \frac{\partial T'}{\partial t}. \tag{7.22}$$

Neglecting the vortex contribution in equation (7.14), we express the superfluid

velocity fluctuation in a second sound wave in terms of the temperature perturbation:

$$\frac{\partial \vec{v}'_s}{\partial t} = -i\,\omega\,\vec{v}'_s = s\,\nabla\,T' \tag{7.23a}$$

or

$$\vec{v}'_s = \frac{i}{\omega}\,s\,\nabla\,T' \,. \tag{7.23b}$$

Using (7.22) and (7.23b) to eliminate the the density perturbation ρ_s' and the velocity component $\vec{v}'_s$, the wave equation (7.20) becomes:

$$\nabla^2 T' + k^2\,T' = -\frac{i}{\rho_s s\,\omega}\left\{ -\omega^2 \left(\frac{\partial \rho_s}{\partial T}\right)_{p,\vec{w}^2} \vec{v}_s \cdot \nabla\,T' \right. \tag{7.24}$$

$$\left. + \frac{\rho_s^2 s}{\rho}\,\nabla\cdot\left[\,\nabla\cdot\left(\vec{v}_s\;\nabla\,T' + \nabla\,T'\;\vec{v}_s\right)\,\right]\right\}.$$

Here, k is the wavenumber, and $\omega = k a_2$.

Equation (7.24) is now in the form of a wave equation with a linear source term on the right hand side. A similarity with the equations obtained in other publications can be noted. The second term is the equivalent of the quadrupole term in Lighthill's [12] formulation of the flow/sound interaction problem. The first term, however, which represents a dependence of the scattering on density variations in the superfluid component, does not seem to have a conventional analog.

We will use the Born approximation in order to solve (7.24). This approximation assumes that the solution of the problem can be written as a perturbation series, in our case:

$$T' = T_0' + T_1' + \cdots, \quad (T_1' << T_0') . \tag{7.25}$$

In this notation, T_0' represents the incident wave, and T_1' is the sought after scattering contribution to the total wave field.

The incident wave has cylindrical character and is modeled as the superposition of plane waves with varying angles of incidence (see Sommerfeld [13]):

$$T_0' = T_i \int_{-\psi_0}^{\psi_0} e^{i\,k\,r\,\cos(\theta - \psi)}\, d\psi . \tag{7.26}$$

The magnitude of the temperature fluctuations in the wave focus is in this formulation $T_i \times 2\psi_0$. It is assumed that the "centerline" of the wave lines up with the x-axis. Then θ is simply the direction of the observer, and ψ_0 gives the wedge half-angle of the focussing wave.

The vortex flow $\vec{v}_s$ is described by a vector, which in cylindrical coordinates has only an azimuthal component in the direction $\hat{e_\varphi}$:

$$\vec{v}_s(\vec{r}) = f(r) \cdot \hat{e_\varphi} . \tag{7.27}$$

Substituting (7.25) - (7.27) into (7.24) gives an equation for T_1' :

$$\nabla^2 T_1' + k^2 T_1' = T_i \frac{1}{a_2} \frac{\rho_s}{\rho} \int_{-\psi_0}^{\psi_0} d\psi \; e^{i k r \cos(\theta - \psi)} \tag{7.28a}$$

$$\left\{ f_1 \sin(\theta - \psi) + i k f_2 \sin\left[2 (\theta - \psi) \right] \right\}.$$

In this equation, the following abbrevations have been introduced:

$$f_1 = -f'' - \frac{f'}{r} + \frac{f}{r^2} + k^2 f \left[2 - \alpha \right]$$

$$f_2 = \frac{f}{r} - f' \tag{7.28b}$$

$$\alpha = - \frac{\rho s T}{\rho_s \rho_n c} \frac{\partial \rho_s}{\partial T} \Bigg|_{p,w^2} = - a_2^2 \frac{\rho}{\rho_s^2 s} \frac{\partial \rho_s}{\partial T} \Bigg|_{p,w^2}.$$

Given a vortex velocity distribution $f(r)$, equation (7.28a) can be solved using the Green's function method. Appendix D outlines the necessary steps.

At this point a short comment on the method of solution seems appropriate. The Born approximation/Green's function approach is not the only way to solve the problem. Several of the cited references [2,8,9] use the method of matched asymptotic expansions, which does not require an a priori decomposition of the perturbation T' into incident and scattered components. Since, however, the incorporation of boundary conditions becomes more difficult in that formalism, we prefer the present method.

In order to obtain the final scattering formula, we have to introduce now a specific vortex profile f. To recapitulate: we assumed in the derivation of (7.28) that $\nabla \cdot \vec{v}_s \equiv 0$ and $\nabla \times \vec{v}_s \equiv 0$. This is consistent with the following potential vortex profile:

$$f(r) = \begin{cases} 0 & (0 < r \leq a) \\ \dfrac{\Gamma}{2\pi r} & (a < r \leq b) \\ 0 & (b < r < \infty) \end{cases} . \qquad (7.29)$$

The truncation at $r = a$ has been introduced for obvious physical reasons. The velocity has to stay finite and reaches a maximum at the core radius a. The solution will be prove to be insensitive to the velocity profile in the core region and the actual value of a. Thus, the choice made is not very crucial.

The vortex flow has to be truncated at an outer radius b for a somewhat more subtle reason. The Born approximation produces a singularity in the forward scattering direction if the vortex is not of finite size. This is usually associated with the breakdown of that approximation for an infinite domain of interaction, because the vortex profile dies out too slowly [4.6]. Fortunately, the present experiment provides a physical length scale that can be used to come up with a value for b. The vortices in rotating helium form a lattice. Their local influence in the rotating frame of reference should thus be limited to about half the intervortex spacing.

Substituting (7.29) back into (7.28b) leads to a solution of the form

$$T_1'(r,\theta) = -\frac{T_i}{2\sqrt{2\pi}} \left(\frac{k\Gamma}{a_2} \right) \frac{\rho_s}{\rho} \frac{1}{\sqrt{kr}} e^{ikr} e^{-i\frac{\pi}{4}} \int_{-\psi_0}^{\psi_0} d\psi$$

$$\left\{ \left[1 - \frac{\alpha}{2} \right] \cot\frac{\theta-\psi}{2} \left[J_0(\kappa a) - J_0(\kappa b) \right] \right. \tag{7.30}$$

$$\left. - 2 \sin(\theta-\psi) \left[\frac{J_1(\kappa a)}{\kappa a} - \frac{J_1(\kappa b)}{\kappa b} \right] \right\}.$$

Here, (r,θ) are the coordinates of the observation point, and $\kappa = 2\,k\,\sin\frac{\theta-\psi}{2}$.

The product κa is for the wavenumber range of the experiment a very small number ($a \approx 10^{-10}$ m, $k \approx 10^{4}$ m^{-1}), so that we can expand the Bessel function containing that term.

The final solution thus becomes

$$T_1'(r,\theta) = - \frac{T_i}{2\sqrt{2\pi}} \left(\frac{k\Gamma}{a_2} \right) \frac{\rho_s}{\rho} \frac{1}{\sqrt{kr}} e^{i k r} e^{-i\frac{\pi}{4}} \int_{-\psi_0}^{\psi_0} d\psi$$

$$\left\{ \left[1 - \frac{\alpha}{2} \right] \cot\frac{\theta-\psi}{2} \left[1 - J_0(\kappa b) \right] \right. \tag{7.31}$$

$$\left. - \sin(\theta-\psi) \left[1 - 2\,\frac{J_1(\kappa b)}{\kappa b} \right] \right\}.$$

In order to get a better understanding of the solution, we write it as

$$\frac{T_1'(r,\theta)}{T_i} = G_1(r) \cdot G_2(\theta) \tag{7.32}$$

where

$$G_1(r) = -\frac{1}{2\sqrt{2\pi}} \left[\frac{k\Gamma}{a_2}\right] \frac{\rho_s}{\rho} \frac{1}{\sqrt{kr}} e^{ikr} e^{-i\frac{\pi}{4}} \tag{7.33a}$$

$$G_2(\theta) = \int_{-\psi_0}^{\psi_0} d\psi \tag{7.33b}$$

$$\left\{ \left[1 - \frac{\alpha}{2}\right] \cot\frac{\theta-\psi}{2} \left[1 - J_0(\kappa b)\right] - \sin(\theta-\psi) \left[1 - 2\frac{J_1(\kappa b)}{\kappa b}\right] \right\}.$$

Figure 7.1 shows the modulus of $G_1(r)$ as a function of temperature, which enters indirectly through the density terms and the speed of second sound. The other parameters were chosen as $\Gamma = 10^{-7}$ m^2s^{-1}, $\omega = ka_2 = 4\pi\times10^5$ s^{-1}, $r = 2.724\times10^{-2}$ m, which represent the values for a typical experiment. Note that G_1 is a decreasing function of temperature and thus mainly dependent on the superfluid density fraction $\frac{\rho_s}{\rho}$.

The next figure, 7.2, shows the temperature dependence of α, which was defined in equation (7.28b). Figure 7.3 depicts the magnitude of G_2, that is the scattering amplitude as a function of the angle of observation with respect to the incident wave. Note the peaks in the forward direction, whose strength is a strong function of the outer vortex radius b . For infinite radius, we almost get two forward scattering singularities, which indicates that the Born approximation breaks down in that case. The dashed lines mark the extent of the incident wave (around $\theta = 0$) and the sector over which two of the sensors in the experiment integrate.

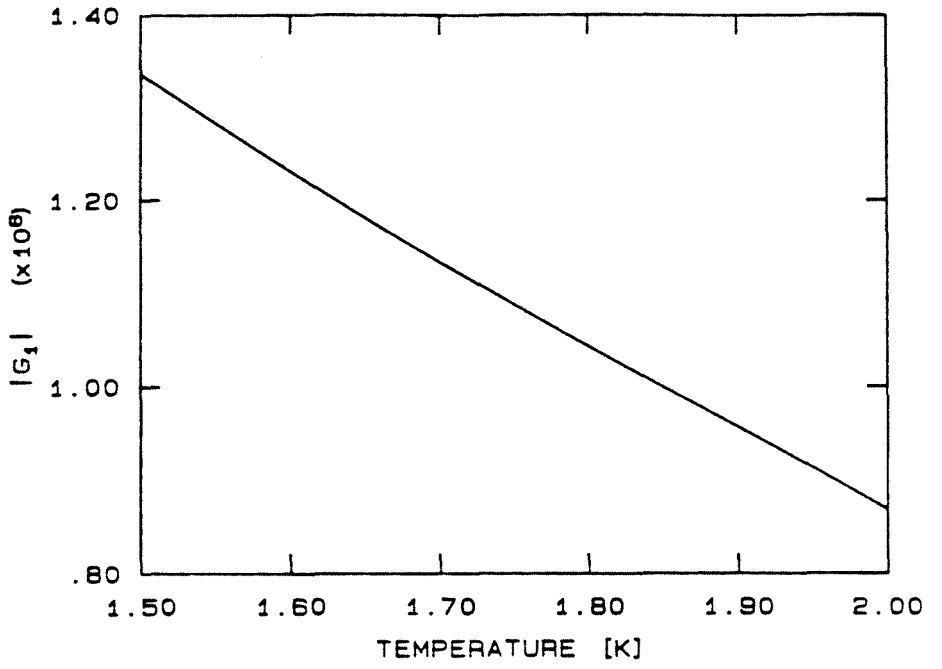

Figure 7.1. Radially dependent part of the scattering response.

We may eliminate the θ - dependence of G_2 by averaging in addition over the solid angle subtended by one of the sensors in the experiment.

$$G_2' = \frac{1}{\theta_2 - \theta_1} \int_{\theta_1}^{\theta_2} d\theta \, G_2(\theta) \tag{7.34}$$

Using the actual values $\theta_1 = 56.48°$, $\theta_2 = 135.43°$, $\psi_0 = 26.19°$ and $b = 2\times10^{-4}$ m, we obtain the result depicted in Figure 7.4.

The product of $| G_1 |$ and $| G'_2 |$ gives finally the scattering amplitude ratio and is depicted in Figure 7.5. For an incident wave of amplitude $T_i = 10^{-3}$ K, the scattered signal picked up by the sensors should be on the order of 10^{-9} K. An additional factor of two is gained by the signal doubling due to reflection of the second sound waves from the sensor surfaces.

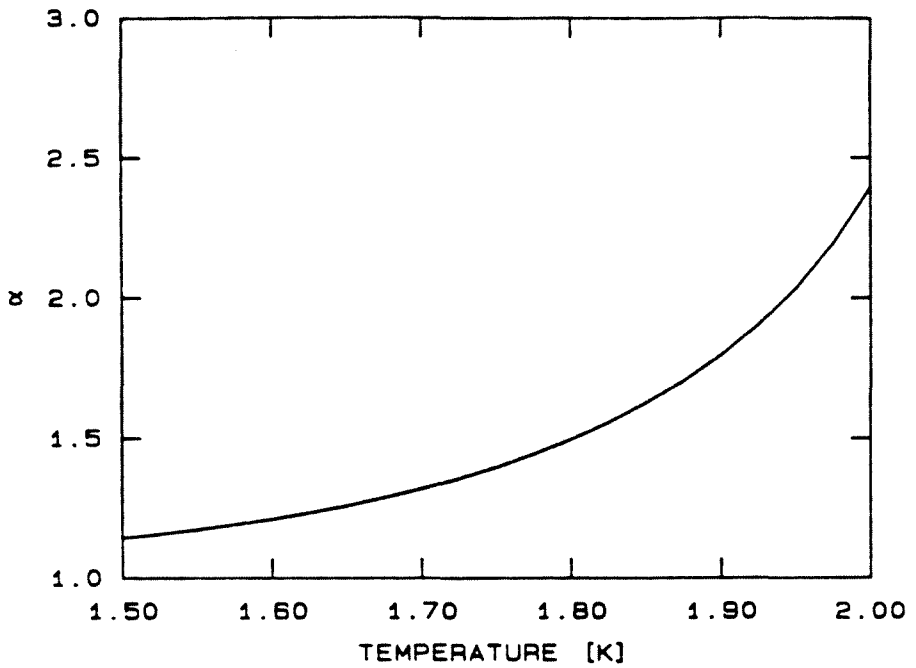

Figure 7.2. Temperature Dependence of $\alpha(T)$

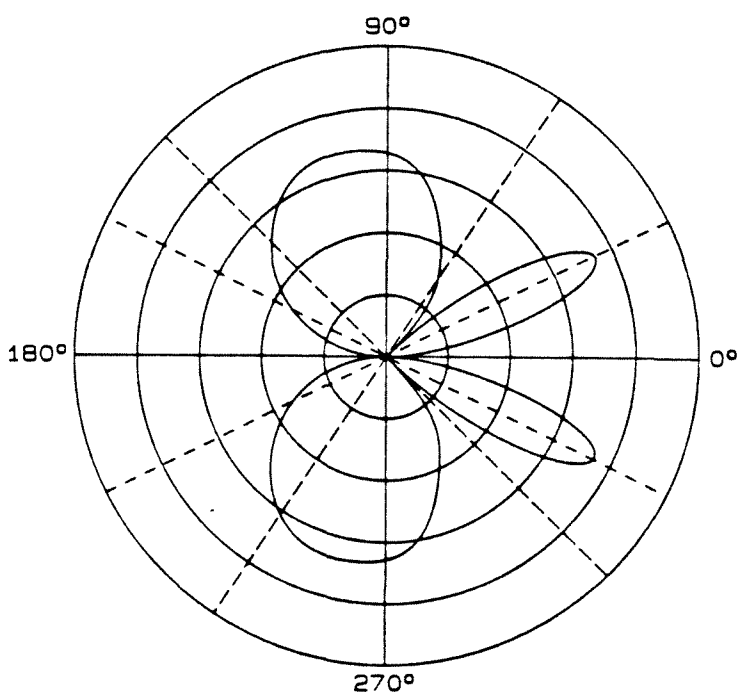

Figure 7.3. Scattering polar diagram $G_2(\Theta)$.

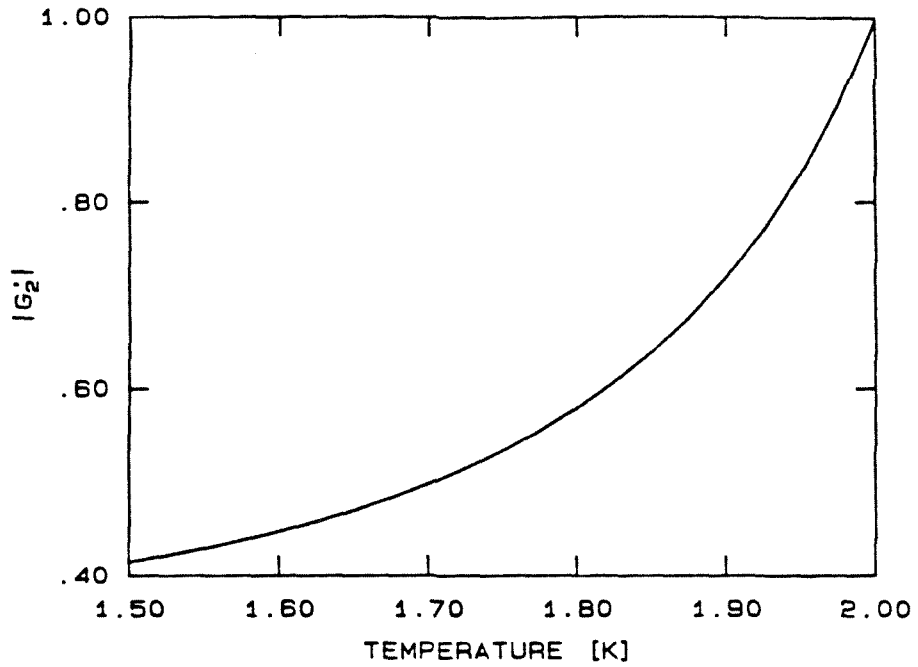

Figure 7.4. Averaged angular response G_2'.

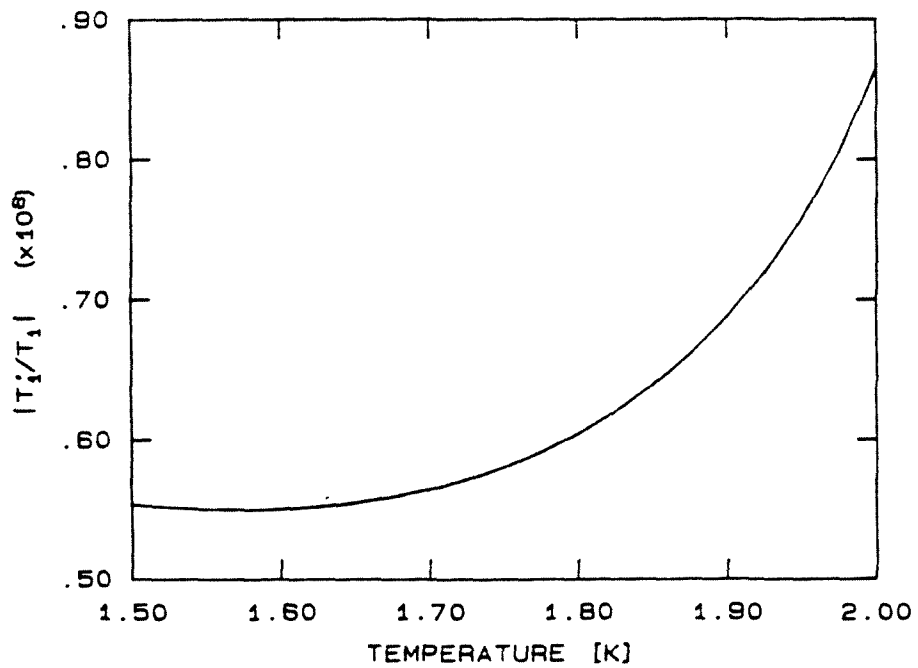

Figure 7.5. Total scattering response.

7.2. Experimental Results

It was hoped that the parabolic cavity would have enough sensitivity to observe some scattering effect associated with the presence of quantized vortex lines.

The experiment was installed in a rotating dewar system which has been described elsewhere [14]. The heater and sensor electronics were the same as described in chapters 5 and 6. The sensor signals were amplified on the rotating table before being fed through mechanical slip-rings into the digital oscilloscope for signal averaging. The operating temperature for all results that will be presented was T = 1.464 K.

In order to estimate the sensor signal response under the experimental conditions, several modifications have to be added to expression (7.31). First, the actual value for the incident wave amplitude T_i may be determined using equation (7.26). Near the focus, one finds

$$T_i = T \frac{T'_f}{2\psi_0} ,$$

with T'_f derived from the heater temperature T'_h as shown in Chapter 6.2. Here, $T'_f \approx 1.42$ mK. At the frequency used in the experiment (f = 100kHz), the second sound attenuation becomes important (see for example Wilks [15]). The numerical value for the coefficient of attenuation is

$$\alpha \approx 3 \times 10^{-13}\ s^2 cm^{-1} .$$

The incident wave amplitude becomes with this

$$T_i = \frac{T_f'}{2\,\psi_0}\, e^{-\alpha\,\omega^2 r_0} = 1.12 \text{ mK} .$$

Here, the heater radius was used as the propagation distance (r_0 = 2.7648 cm) and $\omega = 2\pi f = 2\pi\times 10^5$ s^{-1}. Similarly, the scattered signal will be attenuated on its way to the sensor, reducing the amplitude by a factor

$$\xi = e^{-\alpha\,\omega^2 r_1} = 0.7242$$

with r_1 being the distance focus-sensor (2.7241 cm). At the sensor surface, the temperature fluctuations are doubled due to the wave reflection. Finally, one should look at the vortex line density present in the cavity for the rotation speed Ω used in the experiment (2π s^{-1}). Following the result derived in Appendix C (equation C.18), the number N_f of lines in a circular focal area of diameter $d = \lambda = 2\times 10^{-4}$ m becomes

$$N_f = \frac{2\Omega}{\Gamma}\,\pi\,\frac{\lambda^2}{4} \approx 4 .$$

Using all the corrections mentioned and defining

$$\beta := \frac{T_1'}{T_i} = .4324$$

as the scattering amplitude predicted by equation (7.31), one arrives at the final estimate for the effective sensor fluctuation

$$T_{ens} = T_i \times \beta \times 2 \times N_f \times \xi \approx 2.80\,\text{nK} .$$

Figure 7.6 shows the signals obtained in the parabolic cavity *without* rotation, averaged over 2000 individual bursts. They establish the lower limit of detection, defined here as the root-mean-square of the averaged signals. Using the sensitivities derived in Chapter 6, the amplitude levels are 10.61 nK for sensor S_3 and 4.61 nK for S_2. One sees certain coherent features already in the no-rotation signals. These features are very repeatable and represent probably diffracted waves in the cavity, which become visible only at very large sensitivities. In support of this hypothesis, one may notice that the two sensors do not register similar waveforms. Thus the source of the fluctuations cannot reside in the focal area.

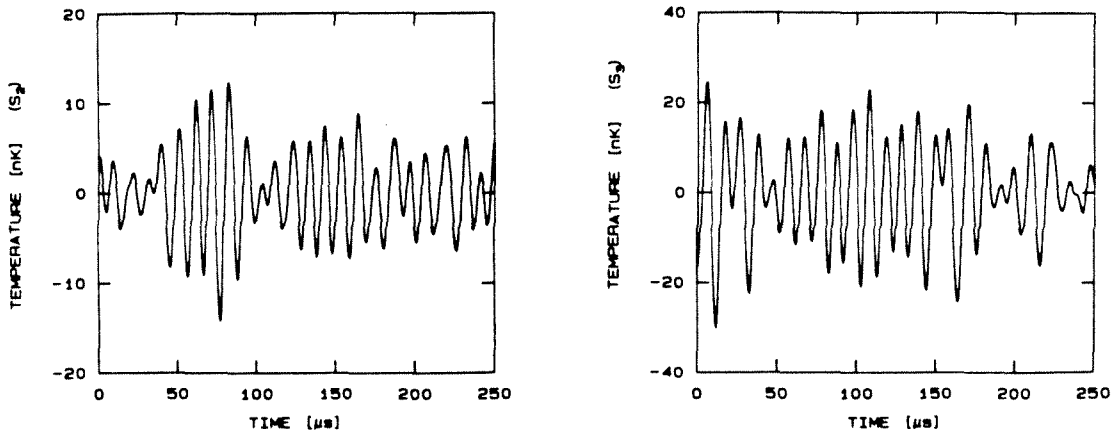

Figure 7.6. Scattering signature in the cavity without rotation.

In Figure 7.7, the results are displayed for the rotating cavity. There seems to be no significant difference compared to Figure 7.6.

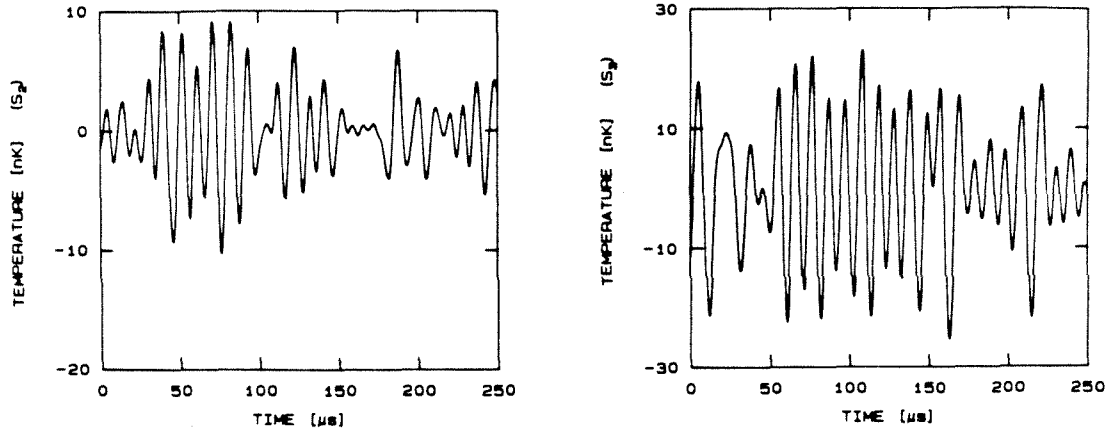

Figure 7.7. Scattering signature for the rotating cavity ($\Omega = 2\pi\ s^{-1}$).

This is demonstrated more clearly in Fig. 7.8, where the *difference* between the rotating and non-rotating signatures (Fig. 7.7 - Fig 7.6) was computed.

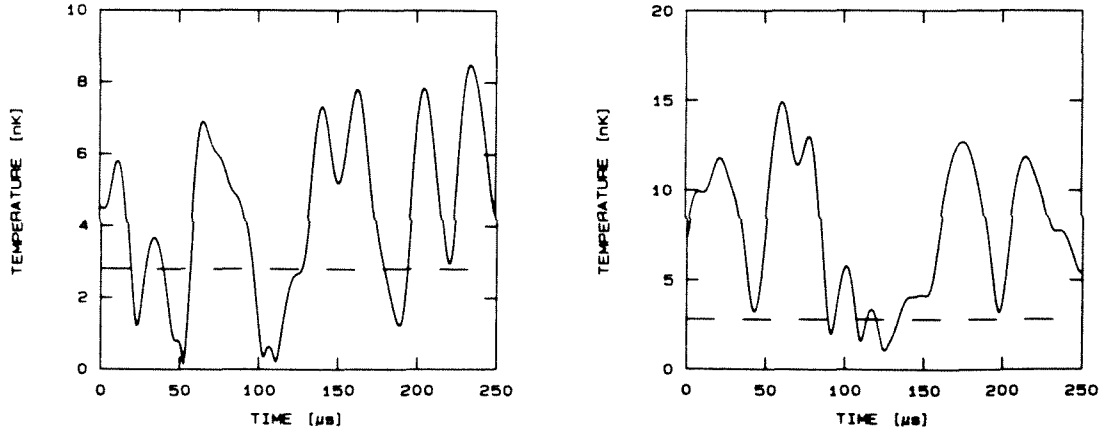

Figure 7.8. Difference between the rotating and non-rotating signatures.

In order to facilitate the comparison with the predicted response, only the signal

envelopes are plotted, following the detection scheme of Chapter 3. The dashed lines indicate the amplitude of a 2.8 nK signal which should be visible as a top hat profile if scattering were observed.

There appear to be no structures in the traces which resemble the expected profile. Thus one has to conclude that scattering from vortex lines cannot be detected in the present cavity. Certain questions arise from this situation. On the one hand, the problem could simply be due to insufficient sensitivities or a somewhat optimistic estimate of the scattering response. On the other hand, however, there could also be more serious difficulties associated with the stability of the vortex lattice. The incident wave is accompanied by a DC counterflow which might drag the vortex line or even destroy it completely. The duration of the counterflow is of course the same as the length of the incident second sound burst, that is a few hundred μs. Assuming that the line is convected with the normal fluid velocity v'_n , the displacement Δl over a time τ becomes

$$\Delta l = v'_n \cdot \tau .$$

The velocity can be estimated based on the definition of the heat flux

$$q = \rho s T v'_n = \rho a_2 c_p T' .$$

Here, ρ is the helium density, s the specific entropy, T the ambient temperature, a_2 the speed of second sound, c_p the specific heat, and T' the temperature perturbation in the counterflow. The numerical values show that the displacement would be a few μm, which is shorter than any characteristic lengthscale of the problem: wavelength, size of the focus or inter-vortex spacing. Thus it seems unlikely that such a displacement would significantly alter the scattering response. Another problem could of course be that the vortex array is unstable

over the averaging time interval (several minutes), leading again to vortex line displacements. This is likely to happen since there are lattice waves in the array with time constants of seconds (see Appendix C). However, the size of the focal area was chosen so as to always contain more than a single vortex line. The scattering amplitude would consequently not be affected by a distortion in the lattice structure, although the phase of the scattering signature might vary enough to reduce the measured average response.

In the light of this, an improvement of the experimental results could come from reducing the averaging times by using a faster signal averager. A general increase in the signal-to-noise ratio would also be helpful. The performance figures of recently developed Gallium-Arsenide transistors (see Appendix F) make them especially attractive for the cryogenic amplifiers in the experiment. Finally, the superconducting materials used in the bolometers should be investigated for possible reductions of the observed thermal time constants (see Chapter 6.1).

7.3. References

1. Müller, E.A. and Matschat, K.R., *The Scattering of Sound by a Single Vortex and by Turbulence*, Technical Report, Max-Planck-Institut für Strömungsforschung, Göttingen (1959).

2. Obermeier, F., *Die Wechselwirkung zwischen Strömungsfeldern und Schallfeldern als singuläres Störungsproblem*, Ph.D. Thesis, Göttingen (1968).

3. Ferziger, J.H., *Low-frequency Acoustic Scattering from a Trailing Vortex*, J. Acoust. Soc. Am. **56**, 6 (1974).

4. O'Shea, S., *Sound Scattering by a Potential Vortex*, Journal of Sound and Vibration **43**, 1 (1975).

5. Yates, J.E., *Application of the Bernoulli Enthalpy Concept to the Study of Vortex Noise and Jet Impingement Noise*, NASA Contractor Report 2987 (1978).

6. Candel, S.M., *Numerical Solution of Wave Scattering Problems in the Parabolic Approximation*, J. Fluid Mech. **90**, 3 (1978).

7. Kambe, T. and Mya Oo, U., *Scattering of Sound by a Vortex Ring*, Journal of the Physical Society of Japan **50**, 10 (1981).

8. Golemshtok, G.M. and Fabrikant, A.L., *Scattering and Amplification of Sound Waves by a Cylindrical Vortex*, Sov. Phys. Acoust. **26**, 3 (1980).

9. Fabrikant, A.L., *Sound Scattering by a Vortex*, Sov. Phys. Acoust. **28**, 5 (1982).

10. Pitaevskii, L.P., *Calculation of the Phonon Part of the Mutual Friction Force in Superfluid Helium*, Soviet Physics JETP **35**, 8 (1959).

11. Fetter, A.L., *Scattering of Sound by a Classical Vortex*, Physical Review **136**, 136 A (1964).

12. Lighthill, M.J., *On Sound Generated Aerodynamically*, Proc. Roy. Soc. London, Series A, **211** (1952).

13. Sommerfeld, A., *Lectures on Theoretical Physics*, Vol. IV (Optics), Academic Press, New York (1954), p. 318 ff.

14. Torczynski, J., *Second Sound Shock Waves In Rotating Superfluid Helium*, Ph.D. Thesis, California Institute of Technology, Pasadena (1983).

15. Wilks, J., *The Properties of Liquid And Solid Helium*, Clarendon Press, Oxford (1967), p. 206 ff.

Chapter 8

CONCLUSION

At the end of the main text, we may now summarize the results described in the previous chapters.

The elliptical cavity was designed to study the feasibility of focused second sound. It demonstrated that complex resonator cavities can be built which have a high enough quality factor to permit several roundtrips of a second sound burst. Scattering from sub-wavelength targets was observed and clearly identified. The agreement with a theoretical estimate was satisfactory, given that certain parameters of the experiment are difficult to control and measure.

The parabolic cavity was able to pick up scattering signals from purely fluid dynamical disturbances, down to the level of 10^{-7} K. The equivalent temperature corresponding to the noise floor was as low as 5×10^{-9}K. The newly developed high impedance sensors showed sensitivities of 500 - 1000 V/K. The effective sensitivities at signal frequencies (100 kHz) were somewhat smaller, but still exceeded several hundred V/K. Cryogenic amplifiers were successfully employed to resolve impedance matching problems associated with the large sensor resistances.

Scattering from individual vortex lines in rotating helium could not be observed. A model to estimate the response of the system for the scattering from vortex lines predicted amplitudes close to the measured fundamental noise level.

Especially this interaction of vortex lines with (second) sound is of substantial scientific interest and should be further investigated theoretically and

experimentally. On the theoretical side, certain phenomena have been described in the literature but could not be discussed within the framework of this thesis. Nevertheless, they appear to be relevant in the general context of vortex scattering. We mention only the possibility of sound amplification by a vortex as indicated in reference [1] and transverse sound waves [2]. Experimentally, the high resistance sensors could be developed further with special attention being paid to their high frequency performance. For the required cryogenic amplifiers, the expanding technology of GaAs-semiconductors seems to carry the greatest promise. All in all, an improvement of the achieved performance limits by an order of magnitude should be possible.

References

1. Golemshtok, G. and Fabrikant, A., *Scattering and Amplification of Sound Waves by a Cylindrical Vortex*, Sov. Phys. Acoust. **26**, 3 (1980).

2. Puttermann, S., *Superfluid Hydrodynamics*, North-Holland / American Elsevier, Amsterdam (1974), p. 145 ff.

Appendix A

Machining of the Cavities

In this appendix we will describe a few aspects of the machining process for both the elliptic and parabolic cavities.

Since the geometry of the resonators is two-dimensional, a numerically controlled milling machine (Bridgeport, with 3-axis controller by Servoproducts, Inc.) was used to cut the desired shapes out of a solid brass piece. The servos have a minimum step size for x,y and z-moves of 0.0005", which is less than $\frac{1}{10}$ of a typical second sound wavelength. The system features automatic backlash compensation so that the tolerances can be maintained even for complicated tool paths. The largest possible diameter for the endmill tool (3/8" for ellipse, 1/4" for parabola) was chosen so as to enhance the surface smoothness.

A FORTRAN program running on a VAX computer generated the data files which contain the tool move commands for the milling machine. For the elliptical cavity a set of 1000 coordinate pairs is computed, describing one-half of one of the ellipses. The rest of the surface is defined using the same data set and the reflection/sign-reversal option of the servo controller. The tool radius correction is performed during the coordinate computation. The coordinate sequences are rounded to the 0.0005" accuracy of the NC system and searched for redundant moves to reduce memory space. Two typical redundant moves are "zero moves," created by the truncation of numbers, and straight line moves defined by more than the starting and end points.

The data set for the parabolic cavity consists of the coordinate pairs for two of the "wings" and the moves describing the circular heater section. The NC

machine has a circular interpolation mode which generates up to 8192 moves from a single command. Thus the heater surface is cut with high accuracy using only a few explicit program steps. Again, the third parabolic section is derived from the initial data set using the symmetry of the design and coordinate reversal. Each parabola is defined by 500 points spaced equidistantly based on the arc length. The same redundancy test as for the ellipse is applied to reduce the length of the data file.

Both cavities have two programs associated with the cutting process: one for the rough cut and one for a finish pass, taking off the last 0.003" during multiple passes along the perimeter. All critical holes are indexed by the machine under program control. Since the workpiece is not removed before this step, accurate alignment of the various parts is assured.

The surface finish of the reflector sidewalls was usually satisfactory already after the finish pass. Some small tool marks associated with the stepping motion of the cutting tool were visible. In the case of the ellipse, they were removed by some light hand polishing. The parabolic cavity could not be treated that way because of the small depth (0.1") of the profile. Although no direct test for the final accuracy of the surfaces was available, tracing of the parabolic cavity with a laser beam showed good agreement with the predicted performance.

As a final note it should be pointed out that the thermal contraction of the metal will change the absolute dimensions of the cavities in the liquid helium environment. However, since this process is isotropic, all geometric features including the focusing behaviour are unaffected.

Appendix B

The Impedance Matching Problem

This section explains two electronic circuits which reduce the capacitive loading effects for high resistance sensors. Due to their different advantages and shortcomings, one of them is better suited for the elliptical cavity and the other for the parabolic resonator.

A coaxial cable has an intrinsic capacitance between its center conductor and outer shield (around 30 pF/ft). This capacitance can lead to severe signal losses when high impedance sources are involved. In Figure B.1, the small signal circuit equivalent is shown for a typical sensor/cable setup with receiving amplifier. The resistor R_B is part of the current biasing circuit, R_S represents the sensor resistance, and C the lumped cable capacitance.

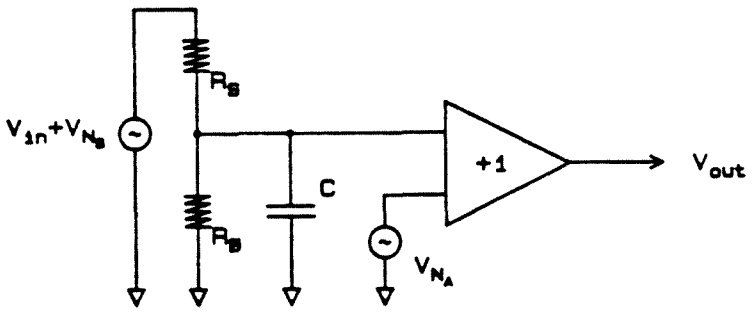

Figure B.1. Circuit equivalent of a sensor / cable / amplifier arrangement.

The amplifier model includes a noise source which contributes a rms voltage V_{N_A} to the overall signal. Similarly, the sensor signal can be split up in a true signal component (V_{in}) and a noise component (V_{N_S}). The output signal becomes

$$V_{out} = (V_{in} + V_{N_S}) \frac{R_B}{R_S + R_B + i\omega C R_S R_B} + V_{N_A} . \qquad (B.1)$$

For very low frequencies, the output signal is simply the input voltage feeding a resistive divider formed by R_S and R_B. On the other hand, using the approximation $R_B >> R_S$ and typical values for R_S (200 kΩ), C (200 pF) and the signal frequency ω (10^6 sec^{-1}), the signal reduction becomes

$$\left| \frac{V_{out}}{V_{in}} \right| \approx \frac{1}{40} . \qquad (B.2)$$

One way of solving this problem is the use of a guard circuit, a schematic of which is presented in Figure B.2.

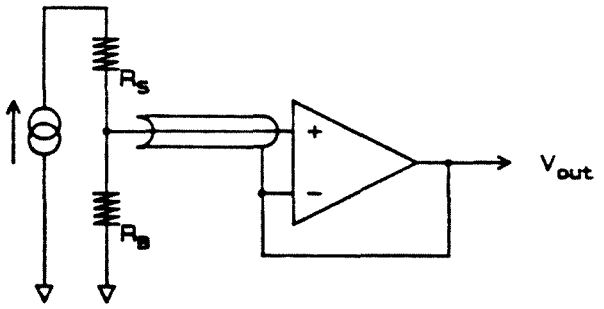

Figure B.2. Schematic of a guard circuit.

A buffer amplifier feeds the received signal back on the coaxial cable shield. Since there is no longer a voltage difference between the center conductor and the shield, the effective capacitance of the cable is reduced. Analyzing the small signal circuit equivalent (see Figure B.3) gives

$$V_{out} = (V_{in} + V_{N_S}) \frac{R_B}{R_B + R_S} + V_{N_A} (1 + \frac{R_B}{R_B + R_S} i\omega C R_S) . \qquad (B.3)$$

Disregarding the noise components for a moment, one sees that the output signal is in this case always determined by the resistive divider: no reduction due to increasing signal frequencies is present. However, if one looks at the signal-to-noise ratio, one finds that it is identical to the one derived from equation (B.1). This is due to the fact that the guard circuit displays positive feedback for the amplifier noise V_{N_A}. The circuit is thus more useful for the wire scattering experiments, where the absolute signal levels are reasonably high and the input frequencies cover a broad range.

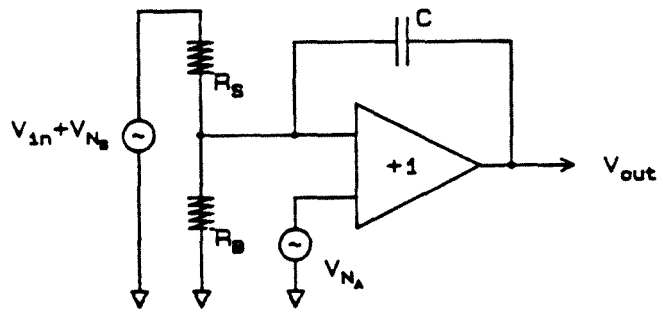

Figure B.3. Equivalent circuit for the guard amplifier system.

For the parabolic cavity, a configuration with a simple line driver/emitter - follower seems more appropriate. In the ideal case, an amplifier with infinite input impedance and small output impedance is used to couple the input signal into the cable. The cable capacitance then becomes unimportant. From the schematic in Figure B.4 one derives

$$V_{out} = (V_{in} + V_{N_S}) \frac{R_B}{R_S + R_B} + V_{N_A} . \qquad (B.4)$$

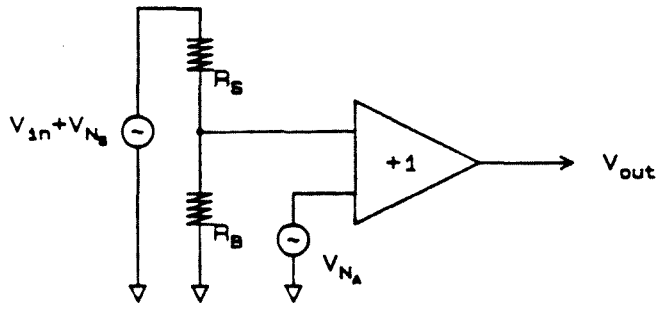

Figure B.4. Equivalent circuit for an emitter follower.

Looking back at equation (B.1) one sees that (B.4) is exactly the same in the limit of vanishing cable capacitance. Again, the signal-to-noise ratio may be calculated as a figure of merit. Normalizing it with the corresponding value for the guard circuit, one finds

$$\xi = \frac{V_{N_S} + V_{N_A}\,(\,1 + i\omega R_S C\,)}{V_{N_S} + V_{N_A}}\,. \tag{B.5}$$

Here, ξ denotes the ratio of the S/N ratios, and $R_B >> R_S$ was assumed. For the parametes used in the experiment, the follower circuit can bring a significant improvement in the signal-to-noise ratio.

Unfortunately, there is one major drawback which makes the use in helium experiments very difficult: the buffer amplifier has to be placed at the beginning of the coaxial cable. This means that it is submerged in liquid helium, an environment where most semiconductors cannot operate. Because of the very attractive features of the follower circuit it was nevertheless employed in the parabolic cavity design, with a special cryogenic transistor serving as the line amplifier.

The problems of operating semiconductors at low temperatures will be discussed in a later appendix.

Appendix C

Vortex Lines in Helium

In this appendix we will summarize some of the features of vortex lines in superfluid helium. The main purpose is to obtain estimates for certain parameters of the experiment, and the derivation of the equations will be kept short. For more details, the reader is referred to textbooks [1-4] or some review papers [5,6].

C.1. Quantization of Circulation

Liquid helium below the λ-transition shows certain peculiar features which have been interpreted as the macroscopic manifestations of quantum mechanics. In order to describe these phenomena, one may introduce a " macroscopic " wavefunction [7] which represents the quantum state of superfluid helium. The wavefunction is written as

$$\psi(\vec{r},t) = \sqrt{\frac{\rho_s(\vec{r},t)}{m_4}}\, e^{i\,\varphi(\vec{r},t)} \qquad (C.1)$$

where ρ_s is the superfluid density, m_4 the mass of a helium atom and φ some as yet unspecified phase function. It is important to note that the wavefunction (C.1) describes the state of superfluid helium as a whole, not the state of single particles.

The product $\psi^* \psi$ gives by definition the number density of "superfluid" helium atoms. The superfluid density in the classical continuum sense then becomes

$$\rho_s(\vec{r},t) = m_4 \psi^* \psi \,. \tag{C.2}$$

In a further step, one introduces a Schrödinger equation

$$i\hbar \frac{\partial \psi}{\partial t} = - \frac{\hbar^2}{2m_4} \nabla^2 \psi + \mu \psi \tag{C.3}$$

where $\hbar$ is Planck's constant divided by 2π, and μ a potential function - it can be identified with the chemical potential of thermodynamics.

Multiplying (C.3) by ψ^*, the complex conjugate of (C.3) by ψ, and subtracting the equations obtained that way gives

$$i \hbar \frac{\partial}{\partial t} \left(\psi^* \psi \right) = - \frac{\hbar^2}{2m_4} \left(\psi^* \nabla^2 \psi - \psi \nabla^2 \psi^* \right) \tag{C.4}$$

or, using (C.2)

$$\frac{\partial \rho_s}{\partial t} = i \frac{\hbar}{2} \nabla \cdot \left(\psi^* \nabla \psi - \psi \nabla \psi^* \right) . \tag{C.5}$$

We identify the right hand side of (C.5) as a flux term and can compare it with the continuity equation of continuum mechanics. It follows that

$$\rho_s \vec{v}_s = - i \frac{\hbar}{2} \left(\psi^* \nabla \psi - \psi \nabla \psi^* \right) . \tag{C.6}$$

Substituting (C.1) into (C.6) gives

$$\vec{v}_s(\vec{r},t) = \frac{\hbar}{m_4} \nabla \varphi(\vec{r},t) \,. \tag{C.7}$$

The superfluid velocity can thus be linked to the spatial gradient of the phase φ of the macroscopic wavefunction. It follows directly that

$$\nabla \times \vec{v}_s \equiv 0 \,; \tag{C.8}$$

that is, the superfluid flow is irrotational.

Considering the circulation inside a circular contour of radius r ,

$$\Gamma = \int \vec{v}_s \cdot d\vec{l} = \int (\nabla \times \vec{v}_s) \cdot d\vec{A} \tag{C.9}$$

we find with (C.7) that

$$\Gamma = \frac{\hbar}{m_4} \int \nabla \varphi \cdot d\vec{l} = \frac{\hbar}{m_4} \Delta\varphi \,. \tag{C.10}$$

Since the integral contour is closed, and φ is a phase function, we can only have

$$\Delta\varphi = N \cdot 2\pi \qquad (N = 0, \pm 1, \pm 2, \cdots) \,. \tag{C.11}$$

and so we finally obtain the quantization condition for the circulation in superfluid helium :

$$\Gamma = N \cdot \frac{h}{m_4} \qquad (N = 0, \pm 1, \pm 2, \cdots) \tag{C.12}$$

The numerical value for $\frac{h}{m_4}$ is 10^{-7} m^2s^{-1}.

C.2. Vortex Lines

A region in which $\Gamma \neq 0$ has to contain a singularity or vortex line. Assuming a rotationally symmetric problem, we find from (C.9) and (C.12) for the azimuthal vortex velocity

$$\Gamma = N \cdot \frac{h}{m_4} = 2\pi\, r\, v_s(r) \tag{C.13}$$

or

$$v_s(r) = \frac{\Gamma}{2\pi\, r}\,. \tag{C.14}$$

This is the flow field generated by a potential vortex. As $r \to 0$, the velocity becomes inifinte. In order to avoid this singularity, one often assumes that a vortex core exists within which the velocity goes to zero. However, in superfluid helium the generally applied viscous core models are not used, since the condition of irrotationality would be violated. It is understood that in helium this condition is *not* an approximation but represents the real behaviour.

One of the more widely accepted models for a quantized vortex line assumes that the superfluid density ρ_s goes to zero inside the vortex core ("hollow core," see, e.g., [5,8]). This means in terms of equation (C.1), that the macroscopic wavefunction has a node in the vortex core. Unfortunately, it seems not possible to derive from this - or from any other core model, for that purpose - a completely consistent estimate for the core size or, equivalently, for the "healing length" of the wavefunction[9]. All theoretical and experimental figures, though,

give numbers for the core size a of about

$$a \approx 2 \times 10^{-10}\ \mathrm{m}\ . \tag{C.15}$$

The core size is believed to increase with temperature and diverges as $T \rightarrow T_\lambda$.

In our scattering calculations (Chapter 7), we will assume a truncated vortex flow; that is $v_s(r) \equiv 0$ for $r \leq a$. This condition is simpler to incorporate in the mathematical formalism and preserves irrotationalty of the flow. As it will turn out, the scattering solution is finally independent of the core radius a, as long as it is sufficiently small.

C.3. Vortex Arrays

In a vessel rotating uniformly with an angular velocity Ω , the fluid undergoes solid body rotation and has a local vorticity

$$\vec{\omega} = \nabla \times \vec{v} = 2\,\vec{\Omega}\ . \tag{C.16}$$

It has been shown experimentally in helium that both the normal and superfluid components participate in this rotation. This apparently violates the condition of zero vorticity for the superfluid. The problem is resolved by creating an array of quantized vortex lines. The array rotates collectively such that the induced velocities approximate solid body rotation, and still $\nabla \times \vec{v}_s = 0$ everywhere except in the vortex cores.

For any finite number of vortex lines, there will be deviations from the linear solid body profile, especially near the vortex cores [10]. In their neighbourhood, the flow supposedly may still be approximated by (C.14). To demonstrate this, Figure (C.1) shows the velocity profile in the center of a rotating cylindrical

vessel containing 100 vortices. The solid line is the induced velocity along the (1,0) "crystalographic" axis of a triangular array of lines in the rotating frame of reference. This result is obtained by summing over the velocity contributions of all vortices and their images. The dashed line represents the velocity field of a single vortex line located at $r = 0$. The plot was generated using the rescaled values $\Gamma = 2\pi$, $\Omega = \frac{2\pi}{\sqrt{3}}$, a minimum vortex spacing of $b = 1$ and a cavity radius $R = 10b$. It turns out that in the regime shown the result stays essentially the same if the radius of the container is increased, while keeping the line density constant.

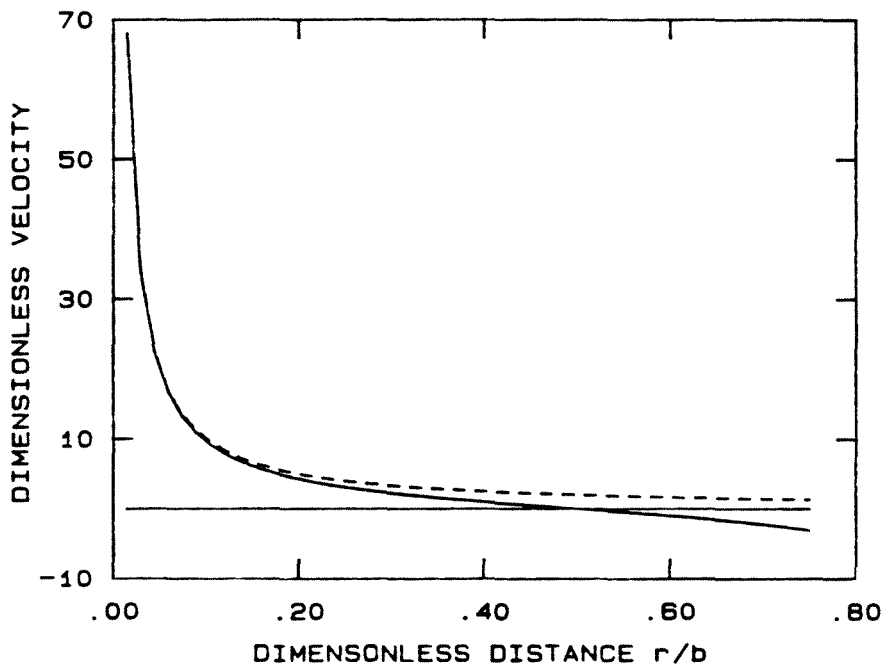

Figure C.1. Velocity profile in a rotating vortex array; the dashed line is the velocity field of a single vortex located at $r = 0$.

In the theoretical considerations mentioned so far, no means is given to determine the actual strength of a single vortex line.

An argument based on the minimization of the energy of the rotating system can be used to show that the most favourable state is one with all vortex lines having unit circulation [11]; i.e., $\Gamma = \frac{h}{m_4}$.

It has been predicted that for a sufficient number of lines the array will have a triangular structure. Visual observations of vortex lines[12], however, and numerical studies[13] seem to indicate that other patterns are more likely to be created.

One can estimate the line "density," that is the number of lines per unit area, by looking again at the circulation around a loop. Postulating that the circulation must be that of fluid rotating with the container, one finds

$$2\,\Omega = N \cdot \Gamma . \tag{C.17}$$

Here, single quanta of circulation Γ were assumed and N is the average vortex line density. If the values $\Omega = 1\ \mathrm{sec}^{-1}$, $\Gamma = 10^{-7}\ \mathrm{m}^2\mathrm{sec}^{-1}$ are used, one obtains a line density of

$$N = \frac{2\,\Omega}{\Gamma} = 2000\ \mathrm{cm}^{-2} . \tag{C.18}$$

This translates into an intervortex spacing of 224 μm, if a square lattice is assumed. For the triangular pattern, the spacing would be somewhat larger. This length may be compared to the wavelength of second sound used in the experiments, which is of the same order.

It should be mentioned that certain metastable states have been observed for the vortex arrays with higher and lower line densities [14]. Thus equation (C.18) is usually seen as giving the equilibrium value for N.

C.4. Vortex Waves

Another topic to be mentioned is vortex waves. The array of vortex lines and the lines themselves are not rigid but execute small oscillations. The point of interest is now whether the second sound scattering from the vortices can be enhanced by coupling into some of the intrinsic wave modes. One usually distinguishes between two modes of wave propagation: waves traveling along the axis of rotation and thus along the vortices, and waves propagating perpendicular to the vortex lines.

The parallel-propagating mode has two interesting limits. For sufficiently small wavelengths, the problem can be treated neglecting vortex-vortex interactions. The dispersion relation in that case is of the form [5]:

$$\omega(k) = \frac{\Gamma}{4\pi} k^2 \left(0.1159 - \ln(ka) \right) . \qquad (C.19)$$

Here, ω is the frequency, Γ the circulation of the vortex line, k the wavenumber and a the vortex core radius. These waves have been investigated experimentally by exciting ions trapped on the vortices with radiowaves [15]. The frequencies involved are in the Megahertz regime. Comparing (C.19) with the linear dispersion relation of second sound, a matching frequency/wavenumber pair cannot be found and coupling of the two waves seems unlikely. If the wavelength is larger than the intervortex spacing, the oscillations become collective and expression (C.19) has to be corrected by adding the now important rotation term 2Ω [16]. These waves have been observed at low frequencies (around 0.1 Hz - 1 Hz), mainly by the damping of torsional oscillations [17,18]. Again, a coupling with second sound is not to be expected.

The perpendicular waves are referred to as 'Tkachenko waves" and exhibit no dispersion. The frequency/wavenumber relation is linear [11,19]

$$\omega = \left(\frac{\Gamma \Omega}{8\pi} \right)^{\frac{1}{2}} k \qquad \text{(C.20)}$$

and the resulting wavespeed is much smaller than that of second sound. Tkachenko waves are measured also in torsional oscillations [20,21].

Recently, the possibility of solitary waves on the vortices has been suggested[22], but there is no experimental evidence yet to support this conjecture.

Summarizing, it can be assumed that second sound will most likely not couple into any of the possible vortex waves.

C.5. Mutual Friction

There is nevertheless a direct interaction between second sound and the vortex lines due to a phenomenon called 'mutual friction." This effect is usually attributed to the scattering of elementary excitations (mainly rotons) from the vortex cores and leads to an additional attenuation of second sound in rotating helium. A recent model [23] suggests a continuum mechanical explanation based on the two-fluid model of a viscous vortex core. At any rate, the vortex lines will be dragged by the counterflow in a second sound beam and undergo oscillations. The periodic displacement might in turn lead to radiation of second sound, in analogy with the case of a classical vibrating vortex[24,25]. The scattering model introduced in Chapter 7 will neglect these effects and assume a steady vortex as a first approximation.

C.6. References

1. Putterman, S.J., *Superfluid Hydrodynamics*, North Holland Publishing Co. (1974).

2. Donnelly, R.J., *Experimental Superfluidity*, Univ. of Chicago Press (1967).

3. Landau, L. and Lifshitz, E., *Fluid Mechanics*, Course of Theoret. Physics, Vol. 6, Ch. 16, Pergamon Press (1979).

4. Tilley, D. and Tilley, J., *Superfluidity and Superconductivity*, Halsted Press (1974).

5. Fetter, A., *Vortices in Helium*, Lectures in Theoret. Physics, Vol. XI-B, Gordon & Breach, Sci. Publishers (1968).

6. Andronikashvili, E. and Mamaladze, Y., *Quantization of Macroscopic Motions and Hydrodynamics of Rotating Helium II*, Rev. Mod. Physics, **38**,4 (1966).

7. Feynman, R., Prog. Low Temp. Physics, **1**, 17 (1955).

8. Harper, J. and Kobe,D., Phys. Rev. B **12**, 1 (1975).

9. Barenghi, C. and Donnelly, R., J. Low Temp. Phys. **52**, 3/4 (1983).

10. Kiknadze, L. and Mamaladze, Y., Sov. J. Low Temp. Phys. **2**, 12 (1976).

11. Tkachenko, V., Sov. Phys. JETP **23**, 6 (1966).

12. Yarmchuck, E. and Packard, R., J. Low Temp. Phys. **46**, 5/6 (1982).

13. Campbell, L. and Ziff, R., Phys. Rev. B **20**, 5 (1979).

14. Mathieu, P., Marechal, J. and Simon, Y., Phys. Rev. B **22**, 9 (1980).

15. Ashton, R. and Glaberson, W., Phys. Rev. Lett.**42**, 16 (1979).

16. Gopal, R., Annals of Physics **29**, (1964).

17. Hall, H., Proc. Roy. Soc. London **A 245**, (1958).

18. Andronikashvili, E. and Tsakadze, D., Sov. Phys. JETP **10**, (1960).

19. Sonin, E., Sov. Phys. JETP **43**, 5 (1976).

20. Isakadze, S., Sov. J. Low Temp. Phys. **4**, (1978).

21. Andereck, C., Chalups, J. and Glaberson, W., Phys. Rev. Lett. **44**, (1980).

22. Maxworthy, T., Barenghi, C. and Donelly, R., private communication.

23. Mathieu, P. and Simon, Y., Phys. Rev. Lett. **45**, 17 (1980).

24. Kop'ev, V. and Leont'ev, E., Sov. Phys. Acoust. **29**, 2 (1983).

25. Broadbent, E., British Aeronautics Research Council, R&M No. 3826, (1976).

Appendix D

Solution of the Scattering Problem

We will outline in this appendix the solution of equation (7.30), using the Green's function method. We will follow the procedure described by Ferziger (see Reference list of Chapter 7, p.73).

The Green's function for a cylindrical, two-dimensional wave problem is

$$g(\vec{r} - \vec{r}') = \frac{i}{4} H_0^{(1)}(k |\vec{r} - \vec{r}'|) \tag{D.1}$$

where a time dependence $e^{-i\omega t}$ has been assumed and the Sommerfeld radiation condition (wave outgoing at infinity) has been enforced.

The solution can then be written as an integral:

$$T_1'(\vec{r}) = - \frac{i}{4} \frac{T_i}{a_{II}} \frac{\rho_s}{\rho} \int_{-\psi_0}^{\psi_0} d\psi$$

$$\int r' \, dr' \, d\varphi \quad H_0^{(1)} (k | \vec{r} - \vec{r}^{\,n} |) \; e^{i k r' \cos(\varphi - \psi)} \tag{D.2}$$

$$\left\{ f_1(r') \sin(\varphi - \psi) + i \, k \, f_2(r') \sin \left[2(\varphi - \psi) \right] \right\}.$$

The functions f_1 and f_2 were defined in (7.28b). Figure D.1 gives a sketch for

the angles ψ, φ and θ.

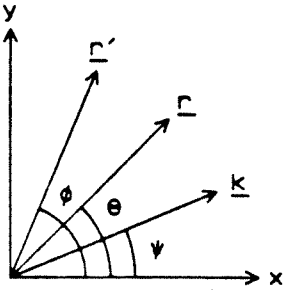

Figure D.1. Geometry for the Scattering Calculations

We use now Graf's addition theorem for the Bessel function[1]:

$$H_0^{(1)}\left(k \mid \vec{r} - \vec{r}' \mid\right) = \sum_{l=-\infty}^{\infty} H_l^{(1)}(kr)\; J_l(kr')\; \cos\left[\, l\,(\theta - \varphi)\,\right] \qquad \text{(D.3)}$$

and the asymptotic expansion as $(kr) \to \infty$

$$H_l^{(1)}(kr) \sim \left[\frac{2}{\pi kr}\right]^{\frac{1}{2}} e^{-i\frac{\pi}{4}}\, e^{ikr}\, e^{-i\pi\frac{l}{2}}. \qquad \text{(D.4)}$$

Upon substitution of (D.4) and (D.3) into (D.2), we obtain

$$T_1'(\vec{r}) = -\frac{i}{4}\,\frac{T_i}{a_{II}}\,\frac{\rho_s}{\rho}\left[\frac{2}{\pi kr}\right]^{\frac{1}{2}} e^{ikr}\, e^{-i\frac{\pi}{4}} \int_{-\psi_0}^{\psi_0} d\psi \int r'\, dr'\, d\varphi$$

$$\left\{ e^{ikr'\cos(\varphi-\psi)}\left[f_1(r')\sin(\varphi-\psi) + ik\, f_2(r')\sin\left[2(\varphi-\psi)\right]\right]\right. \qquad \text{(D.5)}$$

$$\sum_{l=-\infty}^{\infty} e^{-i\pi\frac{l}{2}} J_l(k\tau') \cos\left[l(\theta-\varphi)\right]\Bigg\}.$$

We can first solve the following two integrals:

$$I_1 = \int_0^{2\pi} d\varphi \; e^{ik\tau'\cos(\varphi-\psi)} \cos\left[l(\theta-\varphi)\right] \sin(\varphi-\psi) \qquad \text{(D.6a)}$$

$$I_2 = \int_0^{2\pi} d\varphi \; e^{ik\tau'\cos(\varphi-\psi)} \cos\left[l(\theta-\varphi)\right] \sin\left[2(\varphi-\psi)\right] . \qquad \text{(D.6b)}$$

After some manipulation one obtains:

$$I_1 = -i\,\pi \sin\left[l(\theta-\psi)\right] e^{i\pi\frac{l}{2}} \left[J_{l-1}(k\tau') + J_{l+1}(k\tau')\right] \qquad \text{(D.7a)}$$

$$I_2 = -\pi \sin\left[l(\theta-\psi)\right] e^{i\pi\frac{l}{2}} \left[J_{l-2}(k\tau') - J_{l+2}(k\tau')\right] . \qquad \text{(D.7b)}$$

Equation (D.5) can now be written as

$$T_1'(\vec{r}) = -\frac{\pi}{4}\frac{T_i}{a_{II}}\frac{\rho_s}{\rho}\sqrt{\frac{2}{\pi k r}}\, e^{ikr}\, e^{-i\frac{\pi}{4}} \int_{-\psi_0}^{\psi_0} d\psi \int r'\, dr'$$

$$\Bigg\{\sum_{l=-\infty}^{\infty} J_l(k\tau') \left[f_1(\tau') \sin\left[l(\theta-\psi)\right]\right] \left[J_{l-1} + J_{l+1}\right] \qquad \text{(D.8)}$$

$$+ k\, f_2(\tau') \sin\left[l(\theta-\psi) \right] \left[J_{l-2} - J_{l+2} \right] \Big] \Big\}.$$

We apply Graf's theorem again, with $|k| = |k'| = |\kappa|$ (see also figure D.2 for illustration):

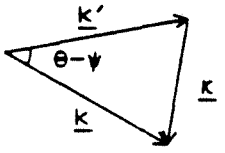

Figure D.2. Relation between the wavevectors k, k' and κ

$$\sum_{l=-\infty}^{\infty} J_l(k\tau')\, J_{l\pm1}(k'\tau') \sin\left[l(\theta-\psi) \right] = J_1(\kappa\tau') \cos\left[\frac{\theta-\psi}{2} \right] \qquad \text{(D.9a)}$$

$$\sum_{l=-\infty}^{\infty} J_l(k\tau')\, J_{l\pm2}(k'\tau') \sin\left[l(\theta-\psi) \right] = \pm\, J_2(\kappa\tau') \sin(\theta-\psi) \qquad \text{(D.9b)}$$

where $\kappa = 2k \sin\dfrac{\theta-\psi}{2}$.

Introducing the equations (D.9) into (D.8), we get

$$T_1'(\vec{r}) = -\frac{1}{2} \frac{T_i}{a_{II}} \frac{\rho_s}{\rho} \left(\frac{2\pi}{k\tau} \right)^{\frac{1}{2}} e^{ik\tau}\, e^{-i\frac{\pi}{4}} \int_{-\psi_0}^{\psi_0} d\psi \int \tau'\, d\tau' \qquad \text{(D.10)}$$

$$\left[f_1(r')\, J_1(\kappa r') \cos\frac{\theta-\psi}{2} - k\, f_2(r')\, J_2(\kappa r') \sin(\theta-\psi) \right] .$$

Using the definitions (7.28b) for f_1 and f_2, as well as the vortex velocity profile (7.29) for f, we arrive again at two integrals:

$$I_1 = \frac{\Gamma}{2\pi} k^2 (2-\alpha) \cos\frac{\theta-\psi}{2} \int_a^b J_1(\kappa r')\, dr' \qquad \text{(D.11a)}$$

$$I_2 = -\frac{\Gamma}{2\pi} (2k) \sin(\theta-\psi) \int_a^b J_2(\kappa r') \frac{1}{r'} dr' . \qquad \text{(D.11b)}$$

Substituting the results back into (D.10) gives the final result, as shown in (7.30):

$$T_1'(r,\theta) = -\frac{T_i}{2\sqrt{2\pi}} \left(\frac{k\Gamma}{a_{II}} \right) \frac{\rho_s}{\rho} \frac{1}{\sqrt{kr}} e^{ikr} e^{-i\frac{\pi}{4}} \int_{-\psi_0}^{\psi_0} d\psi$$

$$\left\{ \left(1 - \frac{\alpha}{2} \right) \cot\frac{\theta-\psi}{2} \left[J_0(\kappa a) - J_0(\kappa b) \right] \right. \qquad \text{(D.12)}$$

$$\left. - 2\sin(\theta-\psi) \left[\frac{J_1(\kappa a)}{\kappa a} - \frac{J_1(\kappa b)}{\kappa b} \right] \right\} .$$

References

1. Abramowitz, M. and Stegun, I., *Handbook of Mathematical Functions*, National Bureau of Standards, Appl. Math. Series, 55, p.363, eq. 9.1.79 .

Appendix E

Fabrication of High Resistance Sensors

The need for high resistance sensors was explained briefly in Chapter 2 and again in Chapter 5 with respect to the parabolic cavity. The simplest way to raise the film resistance is to increase the effective length of the sensor. Whereas values up to several kΩ can still be achieved by mechanically scribing the thin film surface, one has to resort to different techniques to increase these values into the MΩ regime. This appendix will describe the processing steps for the sensors in the parabolic cavity.

Photolithography is used to generate a pattern with a linewidth of 4 μm, which is more or less the smallest scale that can be reliably reproduced in the facilities of the Electrical Engineering Integrated Circuits Laboratory. An important change is made in the basic sensor pattern which for the mechanically scribed devices usually has the shape of a meandering line. The overall sensor size is designed to be approximately .1" × .66". For such a large sensor area it is almost impossible to create a continuous, single 4 micron line. Dust particles which are always present in the air would certainly interrupt the photoresist pattern at many points. Thus a special redundant line pattern was developed that eliminates the problem. Figure E.1 shows a schematic of the pattern element, which is repeated over the length of the sensor. Every loop is bypassed by another one such that only a simultaneous breaking of both parts would destroy the pattern. Taken over the whole sensor, this means a reduction of the achievable maximum resistance by a factor 4. Such a loss in sensitivity is outweighed by the reliability of the manufacturing process: almost all sensors work even with relatively large amounts of dust present.

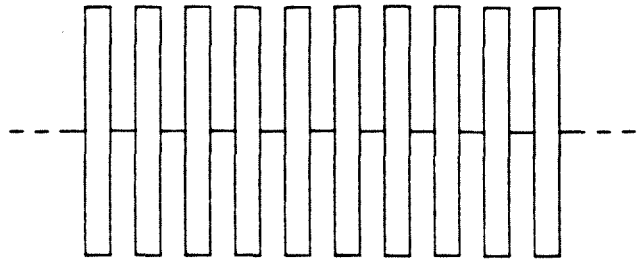

Figure E.1. Schematic of the sensor pattern.

The masks for the photographic processing are produced by scribing an enlarged (× 250) portion of the sensor pattern into a special plastic foil. This material, called "Rubylith" (Ulano Corp., Brooklyn, N.Y.), consists of two plastic layers laminated together. The base layer is transparent whereas the cover layer is opaque to ultraviolet light, which eventually exposes the photographic plates. A large scribing table (1.5 × 2 m) is used to accurately cut out parts of the top layer film. The pattern created this way is reduced photographically by a factor of 25 onto a 2" × 2" photographic plate (Imtech). A second reduction step (× 10) is performed on a 6 barrel photorepeater camera (D.W. Mann Co., Burlington, MA). This camera exposes a 2.5" × 2.5 " photoplate with the first reduction pattern, translates a precise distance and repeates the process. In this fashion, large areas can be exposed, given only a small elementary "cell." In the present case, this cell is a .01" wide section of the sensor line pattern. In a final step, a contact print is made of the developed second photoplate on an iron oxide mask (Oaks Development Lab), which is mechanically more stable than the photoemulsion. Figure E.2 shows a detail of the sensor pattern (the interconnection of the loops on the centerline), as it is seen during the various mask making steps.

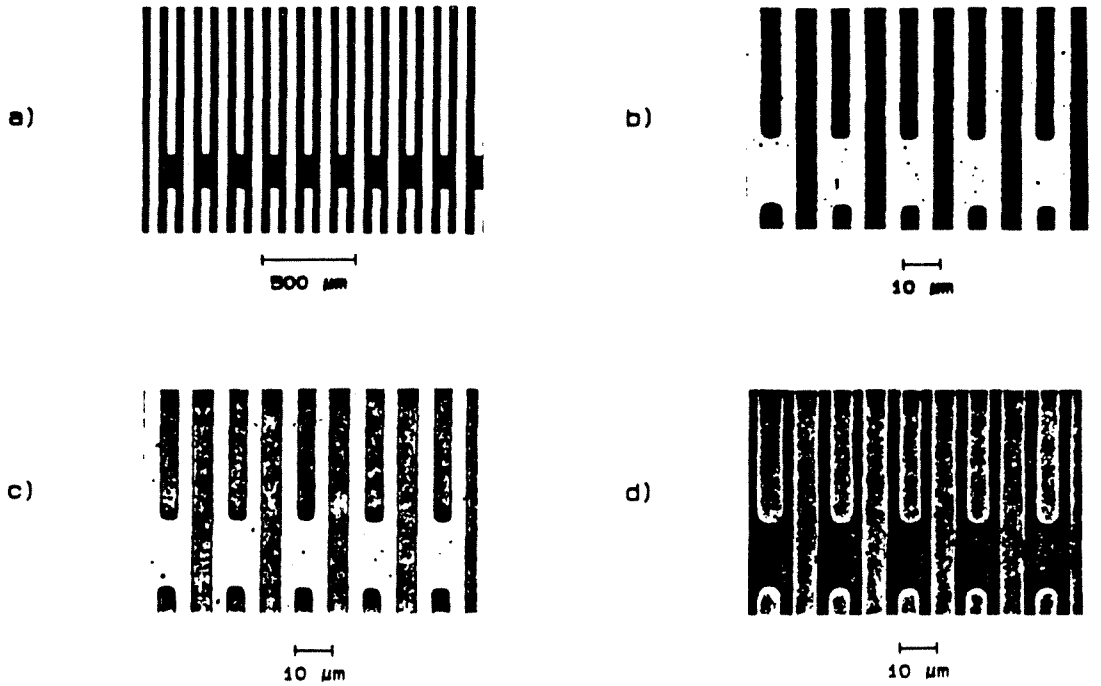

Figure E.2. The sensor masks: first reduction mask (a), second reduction mask (b),iron oxide mask (c) and final photoresist pattern (d).

The photolithographic technique applied is "liftoff" processing. Here, a photoresist pattern is laid out first on the substrate. Then a continuous thin film is evaporated on top. Subsequent dissolution of the photoresist pattern also takes away those parts of the thin film which are not in direct contact with the substrate (see Figure E.3). Compared to the "wet etching" technique, where the pattern is etched out of the thin film through a selective photoresist pattern, the liftoff process gives better dimensional control because undercutting by the etchants is eliminated.

We will now give a summary of the steps involved in making a sensor. The substrates used in the final experiment are Pyrex glass micro slides (Corning, No. 2947), cut to .4" × .95" size. In earlier runs, quartz discs were used. The processing is the same for both materials.

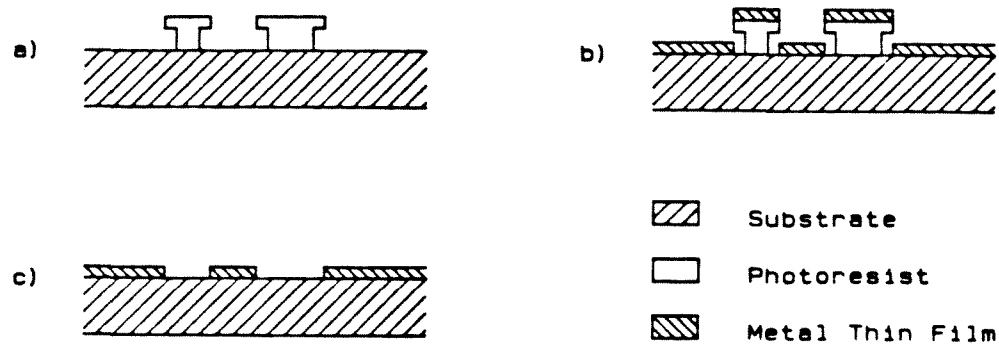

Figure E.3. The liftoff process: substrate with photoresist pattern (a),after thin film deposition (b) and after the removal of the photoresist (c).

— **Cleaning**. After mechanical cleaning in an ultrasound bath, the substrates are soaked in chromerge, sodium hydroxide, methanol and acetone. Immediately before the first film is spun on, a strip cleaning is performed in a plasma oven (oxygen at 600 mTorr for about 20 minutes), that removes readsorbed molecule films.

— **Plastic Film**. A thin polyimide film (Pyralin 2555, Dupont) is deposited on the substrate. This film serves as an adhesion promoter for the photoresist pattern. Since it is self-levelling, it also covers small scratches on the substrate. Finally, due to its very small thermal conductivity, it decouples the sensor material thermally for the substrate, a requirement for high frequency operation of the bolometer. The plastic is spun for 30 seconds at 4000 rpm, creating a film with a thickness of a few μm. After a pre-baking at 125 ^{0}C for 10 minutes, the film is partially cured. A thin layer of positive photoresist (AZ 1350 J, Shipley) is deposited on top of the plastic, and dried for 25 minutes at 85 ^{0}C. The photoresist is exposed with a pattern that marks the areas of the

connecting pads for the sensor. The subsequent development not only removes the photoresist over the sensor pads, but also the underlying polyimide, which is etched away by the developer. Thus, the area of the substrate under the connection pads is exposed again, which is better for the creation of mechanically stable soldering points. The undeveloped photoresist is removed with acetone and the plastic film then cured for several hours at 200 ^{0}C. This hardens the polyimide and makes it resistant to the further chemical/photoresist treatment.

— **Photoresist Pattern**. After curing of the plastic film, photoresist is deposited again for the actual sensor pattern. Spinning a few droplets of AZ 1350 at 4000 rpm for 30 seconds creates a film of a few microns. The thinness of the film is important for the small scales to be created by contact printing. Since impurities in the photoresist solution can spoil large areas of the pattern, the solution is filtered directly before application. The coating is dried for 25 minutes at 85 ^{0}C. The exposure of the sensor pattern is made on a mask aligner (Kasper Instruments, Model 17 A, Mountain View, CA). A mercury arc lamp serves as the light source. In order to facilitate the liftoff process, the *back* of the substrate is flood-exposed first for 2 seconds. This softens the deep lying layers of the photoresist. The actual sensor pattern is created by exposing the *front* side of the substrate for 13 seconds with the iron oxide mask described above. The double exposure produces undercutting of the photoresist during development. This creates a "shadow mask" profile that breaks the metal thin film at the line edges during its deposition. Photoresist development is done for about 45 seconds (Microposit developer, Shipley). After checkout of the pattern under a microscope, further developing can be done, as long as the photoresist is only exposed to safety light. A final flood exposure of the sensor pattern for 30 seconds is performed to guarantee a smooth liftoff. It should be noted in this context that all the given times may

vary depending on the type of light source used, the age of the photoresist, and other uncontrolled parameters.

— **Thin Film Deposition**. The aluminum thin film is evaporated in a vacuum chamber that had been pumped out to about 2×10^{-6} Torr. The mass of high purity aluminum wire is chosen so as to produce a film of 250 Angstrom thickness. The transition temperature is controlled by the pressure of an oxygen atmosphere that is created in the chamber. Since the vacuum pumps are running during this process, a flow equilibrium is set up that supplies oxygen during the evaporation. Partial pressures of about 2×10^{-4} Torr are used to shift the transition of the granular aluminum film to around 1.8 K. More details on the evaporation process can be found in Wise's thesis [1].

— **Liftoff**. The liftoff step is performed by immersing the aluminum film with the underlying photoresist pattern in acetone. This dissolves the photoresist and takes away the aluminum on top of it. A syringe to blow acetone over the surface or a weak ultrasonic bath may be used to assist the process. Even if the liftoff is not complete, the sensor works in many cases since the photoresist pattern effectively breaks the interline connections.

— **Sensor Leads**. The sensor leads are created finally be depositing a comparatively thick copper film on top of the aluminum pattern, using a mask cut into a metal piece. A slight danger exists for losing a sensor due to poor contact between the leads and the aluminum: a thin oxide layer may built up and prevent conduction. However, a sufficiently high voltage across the sensor can usually break through this layer.

In Figure E.4, a microscope picture is shown of an actual sensor film, after the liftoff process has been completed.

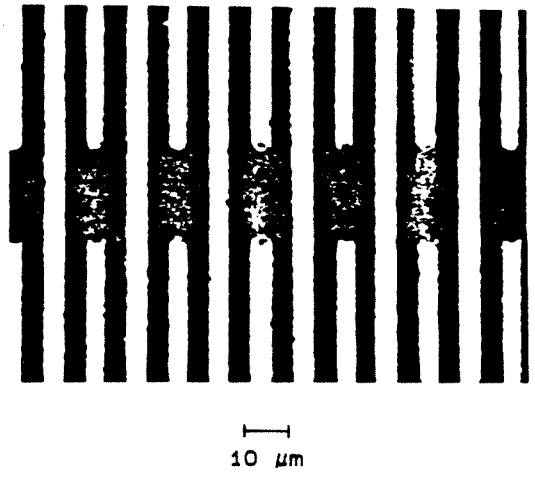

Figure E.4. Photograph of the thin film pattern (magnification 1000×).

References

1. Wise, J., *Experimental Investigation of First- and Second-Sound Shock Waves in Liquid Helium II*, Ph.D. Thesis, Aeronautics, Caltech (1979).

Appendix F

Cryogenic Electronics

In this appendix we will describe some of the underlying problems that led to the construction and use of a cryogenic amplifier stage in the experiment.

The operation of any semiconductor is characterized by the presence of an energy gap and the possibility of charge carriers to bridge that gap by thermal excitation. At low temperatures, the thermal energy available is not large enough any more to create these carriers, and intrinsic semiconductors become insulators. Doped semiconductors show the same effect, although the relevant energy gap is here the difference between the donor and acceptor levels and the band edges. These gaps are a function of the doping levels, that is the number of impurities in the crystal. Silicon-based devices are affected most strongly by the "carrier freeze-out," whereas germanium with its lower energy gap is more suited for cryogenic applications. Finally, there exist certain compounds, for example negatively doped gallium-arsenide (n-GaAs), which should not be affected by freeze-out, because their energy gaps are sufficiently small [1].

Among the transistors only field effect types (FET's) actually operate at helium temperatures. Besides freeze-out, bipolar transistors also suffer from a severe reduction in the minority-carrier lifetime, which makes their operation impossible. FET's, on the other hand, are based on majority carriers and should work, provided that freeze-out does not occur. Thus, germanium or GaAs junction field effect transistors must be considered the most suitable devices for cryogenic applications. Finally there is a group of FET's, which are characterized by an insulated gate (MOSFET), and work by controlling currents through local electric fields. These fields can reach sufficient strength to overcome the

freeze-out and create charge carriers even in silicon-based devices.

The experimental application of the various transistors mentioned is mainly dictated by their availability. Germanium FET's were used some time ago, but are no longer commercially available [2]. Today, almost all field-effect transistors are made with silicon, and consequently, the more recent experiments use MOSFET's as the transistor [3,4]. Within the last few years, GaAs technology has slowly developed so that there are now junction field-effect transistors available that have shown promising behaviour at low temperatures [5].

Another criterion for the selection of a certain type of transistor is its noise performance. Junction FET's are generally quieter than the insulated gate types and would thus be preferable. On the other hand, the gate structure in JFET's permits rather large leakage currents (10 μA). This can become a problem since the sensor bias currents are of the same magnitude and AC coupling would be necessary.

In the present experiment we considered the use of a microwave GaAs junction field effect transistor (GAT 1/010, Plessey Microwave Systems), which has been operated at helium temperatures in the Megahertz frequency range [5]. This device was not readily available at the time, and the final choice consisted in a p-channel silicon MOSFET [6], which had been specifically designed for low noise, low temperature use (ZK 111, Cryoelectronics, Carlsbad, CA). The units were purchased in kit form and assembled at Caltech's Jet Propulsion Lab (JPL). The actual chip was not soldered to the housing but glued with conductive epoxy. This has been shown to reduce significantly the effects of repeated thermal cycling.

The sensors are DC coupled to the transistors, which reduces the number of external low temperature components. The biasing is done with a room

temperature circuit, and only one metal film resistor is immersed in the helium in addition to every sensor/transistor pair. This keeps the dissipation to a minimum. The design of the ZK 111 circuit incorporates the use of a so-called "Night Light." This is a heater wire inside the transistor housing which serves as an infrared emitter and produces extra charge carriers in the transistor substrate. The effect of this is to reduce the noise of the transistor at low frequencies. It was decided not to use this option in the present setup, because its operation in superfluid helium would probably be impaired. Furthermore, the night light causes an increase of the dissipation, and the improvement at higher frequencies seems to be smaller, anyway.

References

1. Lengeler, B., *Semiconductor Devices Suitable for Use in Cryogenic Environments*, Cryogenics, **8** (1979).

2. Arentz, R., *A Brief Characterization of Germanium Junction FETs at 77, 4, and 1.8K*, Technical Report, Society of Photo-Optical Instrumentation Engineers (SPIE), SPIE 364-16 (1982).

3. Petrac, D. and Spencer, R., *Solid-State Circuits for Cryogenic Operation*, NASA Tech Brief **7**, 2 (1982).

4. Petrac, D. and Spencer, R., JPL Invention report NPO - 15255/4782 .

5. Forrest, S. and Sanders, T., *GaAs Junction Field Effect Transistors for Low Temperature Use*, Rev. Sci. Instruments, **49**, 11 (1978).

6. Arentz, R., Hadek, V. and Hoxie, V., *A New Cryogenic P-Channel MOSFET with Optimized Doping...*, Technical Reports, Society of Photo-Optical

Instrumentation Engineers (SPIE), SPIE 364-15 (1982).